www.sciencemag.org/content/345/6192/50/suppl/DC1

Supplementary Material for

Ras activation by SOS: Allosteric regulation by altered fluctuation dynamics

Lars Iversen, Hsiung-Lin Tu, Wan-Chen Lin, Sune M. Christensen, Steven M. Abel, Jeff Iwig, Hung-Jen Wu, Jodi Gureasko, Christopher Rhodes, Rebecca S. Petit, Scott D. Hansen, Peter Thill, Cheng-Han Yu, Dimitrios Stamou, Arup K. Chakraborty, John Kuriyan, Jay T. Groves*

*Corresponding author. E-mail: jtgroves@lbl.gov

Published 4 July 2014, *Science* **345**, 50 (2014)
DOI: 10.1126/science.1250373

This PDF file includes:

Materials and Methods

Figs. S1 to S18

Tables S1 to S4

Full Reference List

Other Supplementary Material for this manuscript includes the following:
(available at www.sciencemag.org/content/345/6192/50/suppl/DC1)

Movies S1 and S2

Materials and Methods

Chemicals

L-α-phosphatidylcholine (95%) (Egg-PC; chicken), 1,2-dioleoyl-sn-glycero-3-phospho-L-serine (DOPS), L-α-phosphatidylinositol-4,5-bisphosphate (PIP_2; Porcine brain), 1,2-dioleoyl-*sn*-glycero-3-phosphoethanolamine-N-[4-(p-maleimidomethyl) cyclohexane-carboxamide] (MCC-PE) were purchased from Avanti Polar Lipids (Alabaster, AL). Texas Red 1,2-dihexadecanoylsn-glycero-3-phosphoethanolamine (TR-DHPE) was purchased from Invitrogen (Carlsbad, CA). Atto647N-maleimide, Atto488-labeled guanosine diphosphate (EDA-GDP-Atto488) and Atto488-labeled guanosine triphosphate non-hydrolyzable analog (EDA-GppNp-Atto488) were purchased from Jena Bioscience (Jena, Germany). Guanosine triphosphate (GTP) was purchased from Sigma-Aldrich (Saint Louis, MO). Guanosine diphosphate (GDP) was purchased from MP Biomedicals (Santa Ana, CA).

Glass substrate cleaning

Chromium corral patterned no. 1.5 thickness glass substrates were prepared by e-beam lithography as described previously (*45*). Prior to use, patterned glass substrates were rinsed individually and bath sonicated in IPA/H_2O 1:1, followed by 3 min piranha etching ($V(H_2SO_4):V(H_2O_2)=3:1$), and thorough rinsing with copious amounts of ultrapure water. *Caution*: piranha solution is hot and highly corrosive and can explode if mixed with organic matter. Appropriate safety equipment is required.

Optical microscopy

Epifluorescence and total internal reflection fluorescence microscopy (TIRFM) images were acquired on a Nikon Eclipse Ti inverted microscope with a 100× 1.49 NA oil immersion TIRF objective and an Andor iXon EMCCD camera (South Windsor, CT). A mercury arc lamp was used for epifluorescence illumination. 488 nm (Sapphire HP; Coherent Inc., Santa Clara, CA) and 647 nm (RCL-050-640; Crystalaser, Reno, NV) laser lines were used for TIRFM imaging. Bandpass emission filters were HQ515/30 and ET630/75 (Chroma Technology Corp., Bellows Falls, VT), respectively. MetaMorph (Molecular Devices Corp., Downington, PA) software was used to control the microscope.

Protein preparation

SOS-HDPC (residues 1–1049), SOScat (residues 566–1049) and SOScat-cyslite (SOScat-C838A, C635A, C980S, E716C) derived from human SOS1 were expressed and purified as described (*10, 12, 19, 46*). Constructs with point mutant(s) were generated using the Quikchange site-directed mutagenesis kit (Stratagene, La Jolla, CA) and confirmed by DNA sequencing. H-Ras(C118S, 1-181) (residues 1–181) and H-Ras(C118S, 1-184) (residues 1-184) were expressed and purified as described (*12, 19*). MS analysis confirmed the identity of the proteins. Fluorescently labeled SOScat-cyslite was prepared by reacting with 10-fold excess of Atto647N-maleimide for 2.5 hrs at 23°C. After labeling, 2 consecutive runs on PD-10 column (GE Healthcare, Pittsburgh, PA) were used to purify labeled SOScat-cyslite from unreacted dye. Degree of labeling was measured by UV/VIS spectroscopy (NanoDrop 2000, Thermo Scientific, Waltham, MA) and calculated to be ~90 %.

Preparation of small unilamellar vesicles (SUVs)

Lipid compositions are given in molar percent. Chloroform mixtures of Egg-PC, MCC-PE, TR-DHPE and DOPS or PIP_2 were dried for 10 min at 40°C in a rotary evaporator followed by drying under a stream of nitrogen gas for 20 min. For DOPS-containing vesicles, mixtures contained 3% DOPS, 3% MCC-PE, 0.01% TR-DHPE, and the balance consisted of Egg-PC; for PIP_2-containing vesicles, mixtures contained 2% PIP_2, 1% MCC-PE, 0.01% TR-DHPE and the balance consisted of Egg-PC. Dried lipid films were resuspended in degassed phosphate buffered saline (PBS, pH 7.45) by vortexing. SUVs were formed by extruding 11 times through a 30 nm polycarbonate filter (EMD Millipore, Billerica, MA) using a hand-held mini-extruder (Avestin, Ottawa, ON, Canada). Vesicles were immediately used to form supported lipid bilayers (SLBs).

Preparation of Ras-conjugated SLBs

SLB formation and experiments were performed in FCS2 flow chambers (Bioptechs, Butler, PA). The patterned substrates were first incubated with maleimide-functionalized vesicles (1 mg/mL in PBS) for 30 minutes, followed by 10 min incubation with Casein (2.5 mg/mL in PBS) and 2.5 hrs incubation with H-Ras(C118S, 1-181) or with H-Ras(C118S, 1-184) (1.3 mg/mL in PBS). Unreacted MCC-PE was quenched by 10 minutes incubation with 2-mercaptoethanol (5 mM in PBS). Samples were thoroughly rinsed at the end of each incubation with 3 mL of PBS buffer. The samples were then cooled to 4°C in a cold room and the buffer exchanged to loading buffer (40 mM HEPES-NaOH (pH 7.4), 150 mM NaCl). Native nucleotide was stripped by 20 minutes incubation with EDTA (50 mM in loading buffer), followed by flushing with loading buffer and overnight incubation with fluorescent nucleotide (10 μM of EDA-GDP-Atto488 or EDA-GppNp-Atto488 in reaction buffer). Reaction buffer is 40 mM HEPES-NaOH (pH 7.4), 100 mM NaCl, 5 mM MgCl2. Next day, Ras-functionalized bilayers loaded with fluorescent nucleotide were brought to room temperature right before use and washed with 3mL reaction buffer under constant flow rate (1mL/min) to remove unbound fluorescent nucleotide. Care was taken to ensure that the SLBs were hydrated at all times.

There is currently no robust method for working with natively lipidated H-Ras in vitro. Purification of native H-Ras (e.g. from insect cells capable of posttranslational modification) results in very limited yields and is severely hampered by hydrolysis and loss of palmitoyl lipid residues (*47*). Semi-synthetic native-like lipidation of Ras superfamily GTPases like Rab and N-Ras has been developed (*48*), but appears intractable for H-Ras (*49*). Maleimido-DOPE coupling to one or two cysteines in the HVR allows native-like membrane coupling of H-Ras, which is fully functional with respect to SOS activation (*19*).

Sample fluidity and Surface density characterization

To assess the quality and surface density of Ras-functionalized supported lipid bilayers, fluorescence fluctuation spectroscopy (FFS) measurements were performed, using a home-built confocal setup based on a Nikon Eclipse TE2000-E inverted microscope (*50*). Two different analytical methods, fluorescence correlation spectroscopy (FCS) and photon counting histogram (PCH) analysis, were applied to analyze measured fluorescence fluctuations. In FCS, time correlation of fluorescence fluctuations were calculated and diffusion coefficients of Ras and TR-DHPE were monitored simultaneously. This allowed us to ensure that both species were laterally mobile (Fig. S1A). PCH analysis allowed us to determine the surface density of Ras accurately since it has the ability to distinguish different clustering states and measure the average density for each state (*51*). In this way, a calibration curve between wide field epifluorescence intensity and Ras density measured by PCH was established (Fig. S1B) and used in later quantification of kinetic traces.

To ensure that Cr corrals were indeed diffusion barriers, fluorescence recovery after photobleaching (FRAP) was performed on a corner of the corral arrays (Fig. S2). Recovery outside the array confirms the lateral fluidity of the membrane (Fig. S2B), while lack of recovery inside the array confirms that Cr lines act as barriers for lateral diffusion (Fig. S2C).

To ensure that Ras-tethered SOS molecules inside corrals were laterally mobile, single molecule tracking of fluorescently labeled SOScat-Atto647N was performed (Fig. S4). SOScat enzymes were seen to remain laterally mobile for the duration of the experiments, sampling the entire surface area of corrals in which they were confined.

Single molecule corral assay

To perform single molecule corral experiments, SOS constructs were injected as a pulse through the system with a flow rate of 2mL/min. To initiate the SOS-mediated exchange reactions, unlabeled nucleotide (GDP or GTP, 120 μM) in reaction buffer together with 1mM TCEP was provided to stably flow through the sample chamber at a flow rate of 1mL/min for first 4 minutes and 0.2mL/min afterwards. Time-lapse epifluorescence images were collected every 35-40 seconds to measure the reaction kinetics for ~20-25 minutes. In the case of Atto647N-SOScat, TIRFM images were taken at the end of the time-lapse recording to show how SOScat diffuses inside the corral.

Corral Occupancy for single molecule activity measurements

In all experiments, SOS surface concentrations were adjusted so that >95% of active (dark) corrals contained only 1 enzyme. During injection through the flow chamber, SOS enzymes bind the membrane surface at random lateral positions. At a given average SOS surface density, the corral occupancy of SOS follows a Poissonian distribution. Therefore, a statistically equivalent requirement to having only a single SOS in an active corral with ~95% probability is that ~10% or less of all corrals in the array are enzymatically active (turn dark) during turnover (Fig. S3). Importantly, this internal control allowed us to reliably monitor single-enzyme kinetics (in >95% of traces) even for non-fluorescent SOS constructs.

Extracting fluorescence decay rates from the corral assay

Epifluorescence images from time-lapse recordings were flattened against reference images acquired outside the corral array, in order to remove intrinsic unevenness caused mainly by the illumination profile (Fig. S5A). Individual kinetic traces were then extracted using a custom algorithm in Matlab, by measuring the average fluorescence intensity from each identified corral in the image, while avoiding corral grid lines (Fig. S5B and C). For further analysis, each kinetic trace from all corrals in the array were normalized to their own initial maximum intensity value, and then corrected for changes in fluorescence intensity due to photobleaching, intrinsic nucleotide release and microscope fluctuations by dividing with the average trace from all corrals without SOS (Fig. S5D). The 'dark corral' (P1) and 'no SOS' (P2) populations were identified in images by the intensity difference between the first and last frames in the time-lapse recordings. For P1, the intensity difference is larger due to a combined effect of SOS-mediated turnover, photobleaching, and intrinsic exchange, whereas for P2 the difference is smaller due to the lack of SOS-mediated catalysis. In the distribution of intensity differences in all corrals in the array, the P2 peak was fitted to a Gaussian curve (Fig. S5E), and a threshold of <0.05 % probability of overlap with the P2 Gaussian was used when defining the P1 population (Fig. S5E and F). Kinetic traces were then separated into the two categories (Fig. S5G).

During the enzymatic reaction, the total Ras density in individual corrals remains constant, and SOS catalysis results in fluorescent Ras becoming non-fluorescent (Fig. S17). As the reaction proceeds, the rate of decrease of fluorescence slows down because a) the density of fluorescent Ras decreases, and b) SOS spends an increasing amount of time turning over non-fluorescent Ras. The result is an exponential decay of fluorescence due to SOS catalysis. Each corral has three potential exponential decay channels:

(1) SOS turnover, k_{SOS}
(2) Photobleaching, k_P
(3) Intrinsic Ras turnover, k_I

For P1,

$$I(t)_{P1} = I_0 \cdot \exp\left(-(k_{SOS} + k_P + k_I)\cdot t\right),$$

whereas for P2,

$$I(t)_{P2} = I_0 \cdot \exp\left(-(k_P + k_I)\cdot t\right)$$

To extract the component of the exponential decay attributable to enzyme catalysis, each kinetic trace of P1 was divided by the average kinetic trace of P2:

$$I(t)_{SOS} = I(t)_{P1} / I(t)_{P2,Avg} = I_0 \cdot \exp\left(-k_{SOS}\cdot t\right)$$

Here, the apparent rate constant k_{SOS} describes the rate of decay of fluorescence due to SOS turning over a constant reservoir of Ras in the presence of a constant concentration of non-fluorescent nucleotide in solution. Calculation of the rate of turnover, TN, from the fluorescence decay rate constant k_{SOS} is explained in the next section.

Dividing the individual traces of P2 with the average trace from all P2 in the array gives corrected baseline traces for zero catalytic turnovers. Both intrinsic nucleotide release and photobleaching involve thousands of Ras in each corral. As a result, in an ideal experimental setup, all empty corrals should decay with nearly identical rates, as stochastic fluctuations in Ras properties are averaged out within each corral. Therefore, differences in fluorescence decay rates between empty corrals mainly result from experimental error. The width of the distribution of decay constants from P2 is therefore used to estimate the minimal distribution width resolvable with the present corral assay experiments.

Extracting molecular kinetic parameters from fluorescence decay rates

The simplest description of the nucleotide exchange reaction catalyzed by one SOS enzyme in the corral assay is characterized by the following reactions:

$$Ras^* + SOS \underset{k_{off}}{\overset{k_{on}}{\rightleftarrows}} Ras^*\cdot SOS \xrightarrow{k_{cat}} Ras^0 + SOS$$

$$Ras^0 + SOS \underset{k_{off}}{\overset{k_{on}}{\rightleftarrows}} Ras^0\cdot SOS \xrightarrow{k_{cat}} Ras^0 + SOS$$

Where Ras^* represents Ras loaded with fluorescent nucleotide, Ras^0 represents Ras loaded with non-fluorescent nucleotide, k_{on} is the association rate constant, k_{off} is the dissociation rate constant, and k_{cat} is the catalytic rate constant. The total number of Ras (R_{Total}) in each corral stays the same and initially all Ras are loaded with fluorescent nucleotide, i.e. $R_{Total} = Ras^*_{(t=0)}$. In the following analysis, we assume SOS-catalyzed exchange does not distinguish between Ras^* and Ras^0. As a result, the probability of SOS catalyzing Ras^0 relative to catalyzing Ras^* during the reaction will be proportional to the numbers of Ras^0 and Ras^*, respectively (Fig. S17).

The reaction scheme can be described with the single molecule Michaelis-Menten equation (*41, 52*):

$$\frac{1}{\langle t \rangle} = k_{cat} \frac{[S]_0}{K_M + [S]_0}$$

Where $\langle t \rangle$ is the mean waiting time between turnovers and $1/\langle t \rangle$ can be interpreted as an average reaction rate (*52*), $[S]_0$ is the substrate concentration and $K_M = \frac{k_{off} + k_{cat}}{k_{on}}$. In the assay, $[S]_0 = R_{Total}$ in each corral. Since the assay measures the rate of fluorescence decrease $-dRas^*(t)/dt$ due to the replacement of Ras^* with Ras^0, the following equation can be used to describe the system:

$$-\frac{dRas^*(t)}{dt} = \frac{1}{\langle t \rangle} = \frac{Ras^*(t)}{R_{Total}} \cdot k_{cat} \cdot \frac{R_{Total}}{K_M + R_{Total}}$$

$$-\frac{dRas^*(t)}{dt} = Ras^*(t) \cdot k_{cat} \cdot \frac{1}{K_M + R_{Total}}$$

$$\begin{aligned} Ras^*(t) &= Ras^*_{(t=0)} \cdot \exp\left[-(k_{cat} \cdot \frac{1}{K_M + R_{Total}} \cdot t) \right] \\ &= Ras^*_{(t=0)} \cdot \exp\left[-(k_{SOS} \cdot t) \right] \end{aligned}$$

with $k_{SOS} = \frac{k_{cat}}{K_M + R_{Total}}$. $Ras^*(t)$ and $Ras^*_{(t=0)}$ represent the number of Ras^* at time t and time 0, respectively, and k_{SOS} is the rate constant for fluorescence decay (per SOS enzyme), as described in the preceding section. To calculate the enzymatic rate (abbreviated here as turnover number, n_T) $n_T = \Delta Ras / \Delta t$ of products catalyzed by one SOS per second we can use the expansion:

$$\begin{aligned} \Delta Ras &= Ras^*_{(t=0)} - Ras^*_{(t)} \\ &= Ras^*_{(t=0)} \cdot (1 - (1 + (-k_{SOS} \cdot t) + \frac{(-k_{SOS} \cdot t)^2}{2!} + \cdots) \\ &\approx Ras^*_{(t=0)} \cdot k_{SOS} \cdot t \end{aligned}$$

when k_{SOS} is small.

For all analysis and discussion, this equation was used to convert apparent rate constants k_{SOS} to enzymatic rates by $n_T = \Delta Ras / \Delta t = k_{SOS} \cdot Ras^*_{(t=0)}$.

This is the general result for k_{SOS} for a SOS mechanism that can be described by the MM equation, and for the turnover number n_T when k_{SOS} is small. The measured k_{SOS} values are in the range of 10^{-4} s^{-1}, justifying omitting the higher order terms in the expansion.

The physical interpretation of k_{SOS} depends on whether Ras density is saturating. In the limiting case where substrate concentration is low, $K_M + R_{Total} \approx K_M$ and $k_{SOS} \approx k_{cat} / K_M$. Conversely, when R_{Total} is saturating and the enzyme k_{cat} becomes rate limiting, $K_M + R_{Total} \approx R_{Total}$ and $k_{SOS} \approx k_{cat} / R_{Total}$. Our results indicate that for all SOS constructs and conditions probed, the rate dependence on R_{Total} is small compared to intrinsic scattering due to variation in k_{cat} and/or K_M (Fig. 3D-F).

In the single molecule assay, individual SOS catalytic states give rise to single-exponential decays of fluorescence intensity, identified as linear segments in log-plots of fluorescence decay over time (Fig. 2A and Fig. S8). Because of the experimental design, this implies that, within the experimental error, SOS does not distinguish between Ras loaded with fluorescent or non-fluorescent nucleotide (Fig. S17). This is true for both the Ras-GDP/GDP-488 and Ras-GTP/GppNp-488 exchange reactions. If SOS displayed a significant difference in activity with respect to Ras loaded with fluorescent or non-fluorescent nucleotides, two exponential terms rather than one would describe each catalytic state.

Identification of individual kinetic states

Distinct kinetic states sampled by individual SOS enzymes were quantified using an unbiased and automated approach. Single-enzyme turnover traces were generally characterized by the presence of a number of well-defined kinetic states, i.e., the enzyme exhibits a characteristic rate of catalysis for a finite time interval and then switches to work at another rate. Evident transitions between such activity states were frequent and, the first step in inferring rates of catalysis from the data was to localize the different states within each trace.

This was achieved using the change point algorithm developed by Ensign and Pande (*23*). The change point algorithm was originally designed for the purpose of identifying transitions in time-series of a stochastic variable spontaneously fluctuating between distinct levels. Change point analysis of the catalysis data was performed after recasting the turnover traces (examples in Fig. S18A and B) in terms of the observed local rate of catalysis (defined as the change in fluorescence intensity between two measured time-points weighted with the time lapsed, Fig. S18C and D). A Bayes factor of 3, generally accepted to reflect ”substantial evidence”, was applied as a criterion in change point identification (*23*). Having localized all statistically significant change points, the apparent turnover rate constant k_{SOS} was obtained for each state as the slope of the least-square fit of the turnover trace to a straight line (black solid lines on Fig. 2A and Fig. S18 and B). The data treatment scheme was implemented in Igor Pro ver. 6.22A (WaveMetrics, Lake Oswego, Oregon, U.S.A.) and operated via a graphical user interface, allowing inspection of the consistency of the identified states and fitted kinetics.

To ensure that transitions between distinct catalytic rates in individual corrals did not arise from SOS enzymes getting stuck in an inactive or sterically inaccessible conformation on bilayer defects or corral walls, diffusion of fluorescently labeled SOScat-Atto647N was imaged simultaneously with catalytic activity (Fig. S10). In order to image SOScat-Atto647N movement over the long time-frame of the experiments (app. 20 minutes) imaging was done at low time-resolution. SOScat was seen to remain mobile within corrals, even as the turnover rate switched between different activity states.

Preparation of SOS schematic in PyMol

The SOS schematic in figure 1A was prepared in PyMol using a SOS-HDPC crystal structure adapted from (12), the HVR region of Ras adapted from (53) and a POPC bilayer structure adapted from (54).

Supplementary Text S1-S7

Supplementary Text S1: Correspondence between single molecule and bulk assays:

Bulk measurements of the apparent turnover rate of SOS (in the absence of membranes) were initially believed to reveal a 10-fold increase in SOS activity when Ras-GTP was bound in the allosteric site, as compared to Ras-GDP in the allosteric site (*6*). Subsequent bulk measurements of the apparent turnover rate of SOS, with Ras bound to saturation in the allosteric site, indicated that the apparent activity of SOS was similar, irrespective of the nucleotide state of Ras (see Fig. S2 in the supplementary material of reference (*10*)). Our single molecule observations of nearly overlapping rate distributions for Ras-GDP and Ras-GTP (Fig. 3) resolve this conflict by showing that Ras-GTP in the allosteric site only mediates a modest, albeit measurable, average increase in SOS specific activity relative to Ras-GDP in the allosteric site (Fig. S13). Importantly, our data reveals that ‘active SOS’ with Ras bound in the allosteric site is not a single state, but represents multiple distinct and interconverting functional states.

Due to the limitation of experimental platforms, earlier kinetic measurements often convolves SOS recruitment of Ras to the allosteric site with any concomitant change in specific activity (*10*): Binding experiments have shown that Ras-GTP has a 7-fold higher affinity for the allosteric site of SOS than Ras-GDP (K_D of 3.6μM compared to 24.5μM respectively) (*10*). At the same time, SOS without any allosteric Ras is ~75-fold less active than SOS with allosteric Ras bound (*55*). Therefore, when Ras and SOS concentrations close to the K_D of the allosteric site were used in bulk assays, nucleotide mediated differences in the extent of Ras binding in the allosteric site were reflected in the apparent rate measurements (*10*). As a result, initial experiments were believed to reveal allosteric effects on the catalytic rate, mediated by the nucleotide state of Ras (*6*). As described above, the single molecule measurements demonstrate that these rate differences were in fact due to different levels of Ras saturation in the allosteric site, rather than an allosteric nucleotide effect. This was also indicated by bulk measurements that used the Ras mutant RasY64A, which only binds in the allosteric site of SOS, to saturate the allosteric site for both Ras-GDP and Ras-GTP. When enough RasY64A-GDP was used to saturate SOS’ allosteric site, the rate difference between Ras-GDP and Ras-GTP was not measurable (see Fig. S2 in the supplementary material of reference (*10*)).

Supplementary Text S2: Conformational dynamics and biochemical regulation

The N-terminal domains of SOS-HDPC auto-inhibit SOS activity relative to SOScat. This is observed as a narrowing of the rate distribution of SOS-HDPC relative to

SOScat, with a large overlap at lower rates (Fig. 2C). These observations are consistent with allosteric regulation by the N-terminal domains via conformational selection (*29-31*). We also observe the dynamics of the effect: the fluctuation frequency observed for SOScat (30%) is significantly lowered in the longer SOS-HDPC and SOS-HDPC(R552G) constructs (10% or less, Fig. S9), showing that allosteric autoinhibition in SOS-HDPC results from suppression of fluctuations that populate multiple high activity states.

For signaling proteins, dynamic properties are likely to play a major regulatory role (*56*). Changes in the internal dynamics of enzymes has been shown to be a potent allosteric modulator of biochemical activity (*24*), via induced changes in the protein conformational entropy (*57*) and via sampling of 'long-lived' poorly populated protein states (*58*). For example, in the Rac GEF Vav1, release of autoinhibition by phosphorylation happens via stochastic fluctuations to a sparsely populated state (*59*). Molecular dynamics (MD) simulations of SOScat predict similar fluctuations in the allosteric and catalytic sites, between inactive and active states, and show that protein flexibility in SOScat may be important for allosteric regulation of SOS (*60*). The functional states observed for SOS in the present work have surprisingly long lifetimes. Protein conformational fluctuations are normally considered to be 'slow' when they happen on the microsecond to millisecond time-scale (*24-26*). However protein states extending this timescale to the seconds range have been observed at the single molecule level (*27*). Historically, ultra long-lived excited protein states have been invoked to explain bulk enzyme hysteresis (*61*) on the minute to hour time-scale (*62, 63*).

Supplementary Text S3: Stochastic simulation of single-state Ras/SOS reaction network

The catalytic cycle of SOS is characterized by a branched network of molecular transitions, related to binding, unbinding and turnover at the two Ras binding sites (*19*). Even in a simplest-case single-state SOScat system, random path selection in this reaction network will lead to stochastic variation in turnover rate over time and between enzymes. In order to estimate the distribution width associated with this variation, we used literature estimates of SOScat rate parameters (*8, 19*) to perform stochastic simulations.

A model was constructed to simulate the interaction of membrane-bound Ras with SOS in the corral assay. We use a convention where "*Ras·SOS"* indicates Ras bound in the allosteric site, "*SOS·Ras"* indicates Ras bound in the catalytic site, and "*Ras·SOS·Ras*" indicates Ras in both allosteric and catalytic sites. *Ras** represents a Ras loaded with fluorescent nucleotide whereas Ras^0 is a Ras with non-fluorescent nucleotide. Our model assumes that SOS is able to switch the binding partners at both allosteric and catalytic sites but only catalyzes nucleotide exchange at the catalytic site. Once a SOS is disengaged from both sites simultaneously it will not be able to bind any Ras again, to simulate the case in the corral assay where a SOS unbinds from surface and is flushed away. Our model contains the reactions shown schematically in figure S11. The rate constants used in the simulation were derived and chosen in order to qualitatively describe the system (*8, 19*).

In this reaction scheme, only channel (I) leads to a nucleotide exchange reaction. On the other hand, channel (II) describes the case where a SOS unbinds from the surface. A stochastic simulation was performed based on the Gillespie algorithm for calculating reaction kinetics (*33*). In this method, the kinetic rate constants are replaced by a set of transition probabilities, p, which define the probability that a single molecule undergoes a conversion from one state to another (*33*).

To generate catalytic traces from stochastic simulations, we assumed that each reaction starts at the upper left corner ($Ras^{*}\cdot SOS\cdot Ras^{0}$) in figure S11 and determined the reaction direction by evaluating the transition probability based on the rate constants (listed below) and a Ras* density of 600 molecules/μm^2. We assume the reaction starts with all Ras bound to fluorescent nucleotide (Ras*) and its initial value can be obtained directly from experiment and used in the simulation. Trajectories were recorded using a time step of 0.06 ms for 500 seconds. After each step, we keep track of and update the position of SOS in the reaction scheme. When the simulation goes through channel (I), a nucleotide exchange event is recorded and the number of Ras* and Ras^0 will be updated. On the other hand, once SOS goes through channel (II) in the reaction scheme, it will stay as (*S*) throughout the simulation and no more exchange would occur since it represents a SOS unbinding event. Under these conditions, one trajectory of Ras* decay over time represents the enzymatic activity observed for a single SOS catalyzing nucleotide exchange in a corral. A total of 500 stochastic simulations were performed and allowed us to extract the corresponding ensemble distribution of kinetics traces.

Rate constants used in the stochastic simulation (details of unit conversion can be found in (*19*): $k_{-A0} = 0.008\ s^{-1}$, $k_{-C0} = 0.008\ s^{-1}$, $k_{A1} = 12000\ s^{-1}$, $k_{-A1} = 6\ s^{-1}$, $k_{C1} = 6000\ s^{-1}$, $k_{-C1} = 5\ s^{-1}$, $k_{cat} = 1.5\ s^{-1}$.

Supplementary Text S4: SOS copy number and variance of ensemble mean

The corral assay reveals that SOS enzymes stochastically fluctuate between long-lived states with catalytic rates that can differ by an order of magnitude or more (Fig. 2B). A fundamental consequence of the broad rate distributions observed for SOS is that average ensemble rates will not meaningfully describe SOS signaling throughput in a cascade if it is mediated by a low number of enzymes, or by enzymes that remain spatially separated on the cell membrane in distinct signaling clusters or membrane compartments. To quantify this behavior, we parameterized the rate histograms for SOS-HDPC bound to either Ras-GTP or Ras-GDP in the allosteric site, by fitting with Lorenzian probability distribution functions. In order to simulate the average and variance of SOS activity as a function of copy number, a certain number n of SOS molecules were randomly selected from the underlying Lorenzian distribution and the corresponding average and variance were computed. This operation was repeated 10,000 times in order to plot the distribution of rate averages for that particular copy number. A selection of resulting average rate distributions are shown for SOS-HDPC-Ras-GDP and SOS-HDPC-Ras-GTP in figure S13A and B. When n=1 the ‘average’ rate distribution is the same as the real rate distribution measured in the corral assay. As n increases, the averaging of individual SOS rates in the growing ensembles tends to narrow the resulting average rate distributions, making the average rate increasingly well defined. These are simple statistical consequences of starting from a wide rate distribution. The significance for interpreting the nucleotide sensitivity of SOS is illustrated in figure S13C, which shows the computed average and standard deviation as a function of copy number for SOS-HDPC: only when the overall activity of a larger ensemble of SOS enzymes mediates the biological signal (~1000) will the variance be low enough for the average rate to accurately characterize the biochemical flux.

For example, GTP has a modest average activating effect on SOS-HDPC (~50% rate increase) (Fig. S13C). This increase is swamped by stochastic noise at low copy number, due to intrinsic rate fluctuations of more than an order of magnitude. This does not mean that there is no nucleotide specificity at low SOS copy number, only that in this regime average rates do not capture the stochastic nature of the observed molecular behavior.

In general, in the low copy number regime, the shapes of the underlying distributions, rather than their global averages, can potentially encode the biological significance of enzyme activity. For SOS, an apparently subtle difference in the ensemble-averaged rate contains a profound difference in the processive capacity of a specific subset of molecules (Fig. 3D-F). This behavior can have large effects on the signaling network in which SOS operates (See supplementary text S5).

Supplementary Text S5: Lateral partitioning of Ras and SOS on the cell membrane

In vivo, Ras proteins are heterogeneously distributed on cellular membranes (*64*). The plasma membrane is organized into compartments by the engagement of transmembrane proteins with the submembrane cortical actin mesh (*65*). Long-range diffusion across multiple compartments is impeded by cytoskeletal boundaries, which have been shown to corral Ras within the membrane (*66*). Within compartments Ras proteins are further partitioned into dynamic domains (*67*) and Ras nanoclusters (*68*), resulting in localized Ras 'hot-spots' on the membrane (*69*). It is therefore likely that the lateral distribution of SOS molecules engaged with Ras on the cell membrane will be similarly heterogeneous, shaped by the spatial pattern of Ras. Indeed, co-regulated spatial patterns of GTPases like Ras, and their cognate activators (GEFs) and deactivators (GAPs) within the cell and on membranes are believed to functionally affect the signaling cascades of these molecules (*36*). As a result of such a heterogeneous distribution of Ras, and likely also SOS, the membrane may not rapidly average the contributions of spatially distinct signaling bursts, leading instead to localized signal propagation from the membrane into the cell (*38*). Under such conditions, a broad distribution of SOS states within the ensemble of enzymes bound to Ras on the membrane, as observed in the corral assay, can lead to localized signaling from regions with SOS in a highly active and long-lived state.

Supplementary Text S6: Modeling SOS rate fluctuations and stochastic signaling dynamics

To gain insight into effects of slowly fluctuating enzyme kinetics, we study a simple model that captures qualitative features of the experimentally measured rate distributions. Consider a single enzyme that can sample three catalytic states: slow, intermediate, and fast kinetics. The enzyme catalyzes the reaction:

$$S \xrightarrow{k_i} S^*$$

where S (the substrate molecule) can be regarded as Ras-GDP, S^* can be regarded as Ras-GTP, and the reaction rate k_i can take on three different values associated with different catalytic states of the enzyme. The values of k_i are chosen to give substrate turnover rates similar to those measured in experiments. The enzyme stays in a given catalytic state for a random time drawn from the exponential distribution with rate γ_S, which we call the switching rate. At the end of each random time interval, the enzyme updates its catalytic state according to the probability distribution associated with the three catalytic states. We denote the probability of being in state i by p_i. Both the value of γ_S and the distribution of kinetic rates depend on the nucleotide occupancy of Ras in the allosteric pocket of SOS. When multiple enzymes are present, each enzyme samples from the same distribution of catalytic rates, and each independently switches catalytic states at random times governed by γ_S. The total rate at which S is converted to $S^*$is given by the sum of the individual enzyme rates.

We also consider conversion of S^* to S, which is mediated by a deactivating enzyme G. This can be regarded as RasGAP activity that catalyzes the conversion of Ras-GTP (S^*) to Ras-GDP (S):

$$S^* + G \longrightarrow S^*G \xrightarrow{k_d} S + G$$

We assume that the binding step happens instantaneously. When the number of S^* exceeds the number of G, the total rate of conversion of S^* to S is constant, giving a zero-order kinetics regime in which the number of S^* does not affect the total rate. The total deactivation rate is 4 s^{-1} (Fig. 4A) or 10 s^{-1} (Fig. 4B) when all deactivating enzymes are bound to S^*. Distributions in Fig. 4B result from trajectories sampled at 100 s. In the results presented below, we use experimentally motivated parameters, with k_1 = 10^{-4} s^{-1}, k_2 = 10^{-3} s^{-1}, k_3 = 10^{-2} s^{-1}, and the total number of substrate molecules, N_{tot}= 10^3.

We use computational methods that account for the stochastic nature of chemical kinetics, simulating the chemical reaction network with fluctuating enzyme kinetics using the Gillespie algorithm (*33*). Each independent simulation gives a trajectory that specifies the number of each type of molecule as a function of time. We track the number of S^* molecules, N_{S^*}, as a function of time. One quantity of interest is the probability that the number of S^* has exceeded a threshold value (N_{thresh}) by time t, which we denote by $\phi(t;N_{thresh})$. The threshold can be regarded as a concentration of Ras-GTP required for activation of a downstream signaling cascade. We calculate $\phi(t;N_{thresh})$ by determining the fraction of trajectories that have reached a threshold value of S^* by time t. Our computational model allows us to study two effects associated with the allosteric influence of Ras-GTP on SOS: (i) increased weight in the high-rate tail of the enzymatic rate distribution and (ii) decreased rate of switching between enzymatic rates.

For a collection of independent enzymes, placing additional weight in the highly active tail of the distribution can lead to fast activation by a subset of the enzymes. In the presence of deactivating enzymes, this can occur even when a collection of enzymes operating at the increased average catalytic rate are unable to support activation (Fig. 4A). Additionally, two molecules with identical enzymatic rate distributions can lead to different ``downstream" signaling signatures if they sample from the turnover rate distribution with different switching rates (Fig. 4B). In particular, we demonstrate that slower switching between turnover rates can lead to a faster response, and that slow switching can promote activation in cases in which fast switching abrogates activation. Here, we fix the distribution of enzymatic rates (p_1= 0.25, p_2 = 0.5, p_3= 0.25) and vary the switching rate γ_S. At times much shorter than γ_S^{-1}, an enzyme is unlikely to switch states and as a consequence the switching rate has a negligible effect on the distribution of N_{S^*} at short times. At times much longer than γ_S^{-1}, one expects the distribution of N_{S^*} to have a single mode that grows as if governed by the average catalytic rate. Hence, different values of γ_S are expected to affect the production of S^* differently at intermediate times.

Figure S16 illustrates how the switching rate affects the distribution of the number of S^* as a function of time when no deactivating enzymes are present. At short times (Fig. S16A), for both switching rates considered (orange and green graphs), there are three peaks associated with the three distinct enzymatic states. However, for slow switching (γ_S = 0.01 s^{-1}, orange), highly active enzymes stay in that state for longer times on average. Hence, there exist trajectories that produce S^* at a high rate for long times, leading to a population of trajectories with large numbers of S^*. For example, consider the histograms at 100 s (Fig. S16B). With γ_S = 0.1 s^{-1} (green), each enzyme has changed catalytic state on average about 10 times. This leads to a blurring of the three peaks seen at the short timescale in figure S16A. However, for the case with γ_S = 0.01 s^{-1} (orange), there are still three distinct peaks, with the peak at large S^* existing at values of S^* that have not yet been sampled with γ_S = 0.1 s^{-1}.

Figure 4A in the main text emphasizes this point by showing that in the presence of deactivating enzymes, slow switching between catalytic states can promote the ability to reach a signaling threshold. Note that when the enzyme operates at the average rate and in the case of fast switching, threshold crossing is completely suppressed, while slow switching allows threshold crossing. Physically, this is because molecules in the highly active state stay in that state longer on average, thus promoting the ability of those enzymes to activate sufficient numbers of S^*.

Supplementary Text S7: Coarse-grained modeling of SOS network dynamics

To study the effects of fluctuating kinetics on the bimodal response of Ras activation in lymphocytes, we performed a coarse-grained, stochastic simulations of the network using the Gillespie algorithm (*33*). The model we employed has been successfully used to interpret bimodal SOS signaling in thymocytes in vivo (*8*). Stochastic simulations were carried out inside a simulation box with an area of $4\mu m^2$ total volume of $V=0.08\mu m^3$. We have chosen the volume in such a way that diffusion within the box is much faster than the time scales of the chemical reactions. Thus, we can assume the simulation box is well mixed. We assume that cytosolic species such as ligand can interact with the membrane bound species only when it has come within a confinement length of d=1.7 nm.

We allow each SOS enzyme to independently switch its catalytic rate with a switching rate γ_S that depends on the allosteric occupancy. At switching times which are stochastically determined in the simulation, the enzyme redraws a catalytic rate from a distribution outlined in table S1-S4, chosen such that the average value is the value recorded in the literature.

In our simulations, we sought to understand and isolate the relative effects of both a heavier tailed distribution and a slower switching rate for SOS with Ras-GTP versus Ras-GDP allosterically bound (hereafter referred to as SOS-Ras-GTP and SOS-Ras-GDP respectively). By switching rate we refer here to the rate at which SOS stochastically draws a new catalytic rate. In our simulation, we consider a simple model in which the catalytic rate of SOS is allowed to fluctuate between a discrete set of states with probabilities chosen such that the average catalytic rate coincides with experimentally known values (Supplementary table 1 and 2). We allow the SOS enzyme to draw from different catalytic distributions based on the allosteric occupancy. The amount of time that a SOS enzyme will remain in one catalytic state is itself a random variable governed by the aforementioned switching rate (Supplementary table 3).

Our simulations suggest that there are two main results of allowing a fluctuating catalytic rate. First of all, the range of SOS concentrations that elicits a bimodal response is shifted to higher values when compared to the case of a non-fluctuating SOS catalytic rate (Figure 4C). This implies that the Ras/SOS network with rate fluctuations becomes more conservative in the sense that greater signal strength (as measured by SOS concentration) is required to elicit a high Ras-GTP level. The second main result is that the range of SOS concentrations corresponding to a bimodal response is widened (Figure 4D).

These results are both due to the heavy-tailed nature of the catalytic distribution of SOS-Ras-GTP. Because the enzyme can sample catalytic rates below the average value with high probability, the effective concentration of SOS-Ras-GTP appears lower than the case in which there is no rate fluctuation. Having a slower switching rate for SOS-Ras-GTP versus SOS-Ras-GDP exaggerates this effect when compared to the case of equal switching rates, and pushes the bimodal response to even higher values of SOS concentration (Figure 4C). This is because the enzyme now lingers on slow catalytic rates for a longer expected time due to the slow switch rate. Because of the heavy-tailed nature of the distribution, the states slower than the average have relatively high probability.

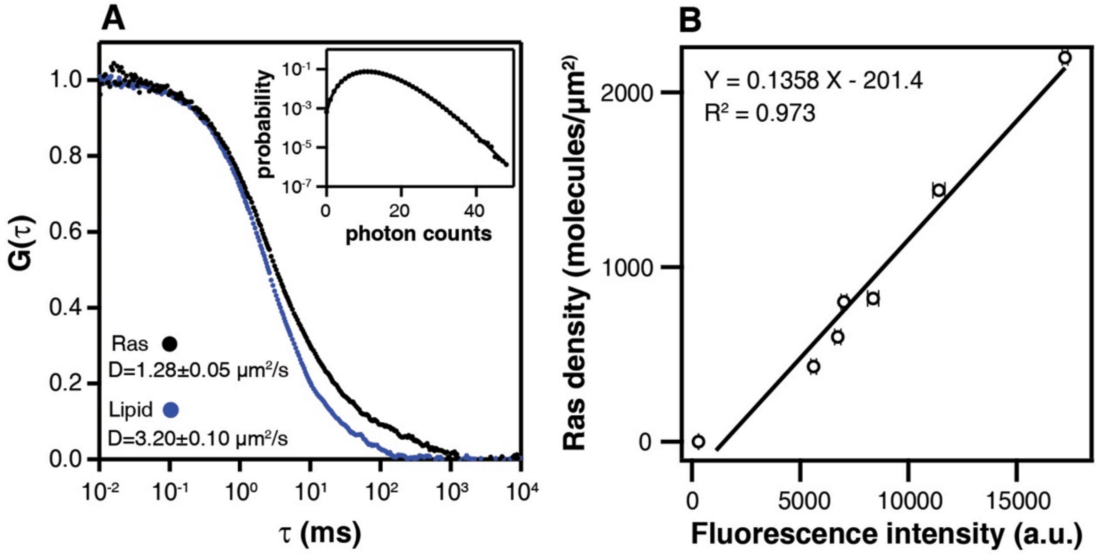

Fig. S1. Sample fluidity and Ras surface density.

(A) Normalized auto-correlation functions, G(t), of H-Ras and TR-DHPE lipid measured simultaneously. Ras displays a slower lateral diffusion compared to lipid. Insert, PCH analysis for Ras on the surface. The PCH analysis gives a surface density of 592 Ras/μm2. (B) Calibration curve for the conversion between fluorescence intensity and Ras density. Ras density was determined by PCH analysis.

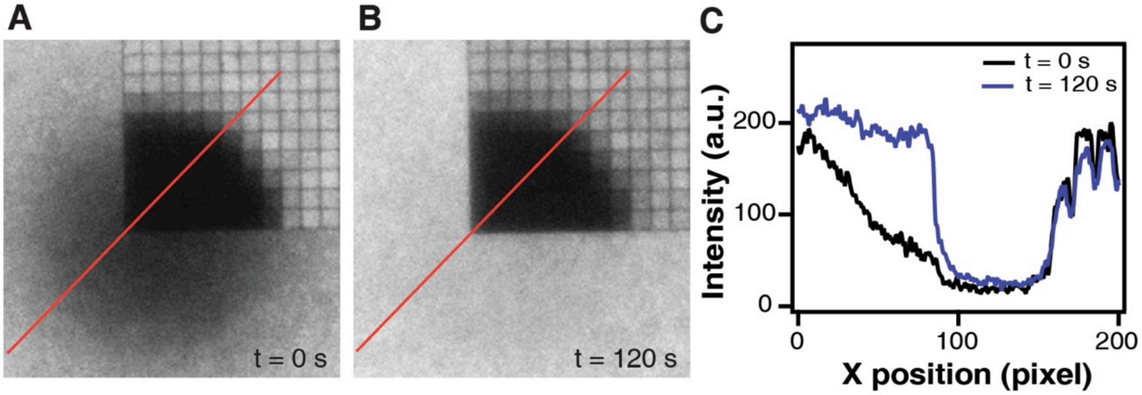

Fig. S2. Fluorescence recovery after photobleaching (FRAP) characterization of Ras mobility.

(A) FRAP was performed at the corner of an array of corrals. (B) No fluorescence recovery was observed inside the corral array area due to the chromium diffusion barriers. The bleached area outside the array recovered fluorescence as laterally mobile Ras molecules diffused into the bleached spot. (C) The fluorescence intensity plot along the red cross section in (A) and (B) shows the fluidity of the sample.

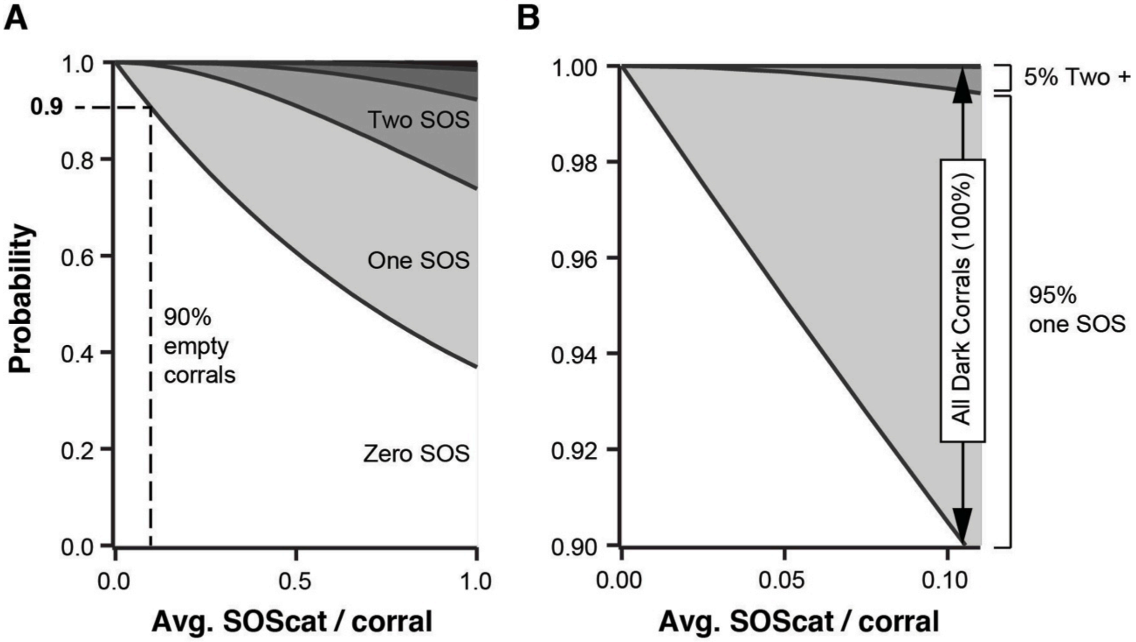

Fig. S3. Poissonian statistics of corral occupancy.

(A) Assuming random binding of SOS from solution onto discrete corrals, a mean occupancy of ~ 0.1 SOS/corral (vertical dotted line) will correspond to 90% of all corrals being empty. (B) Of the ~ 10% of corrals that contain SOS enzyme (full vertical arrow), 95% will contain only 1 SOS, while 5% will contain 2 or more SOS molecules.

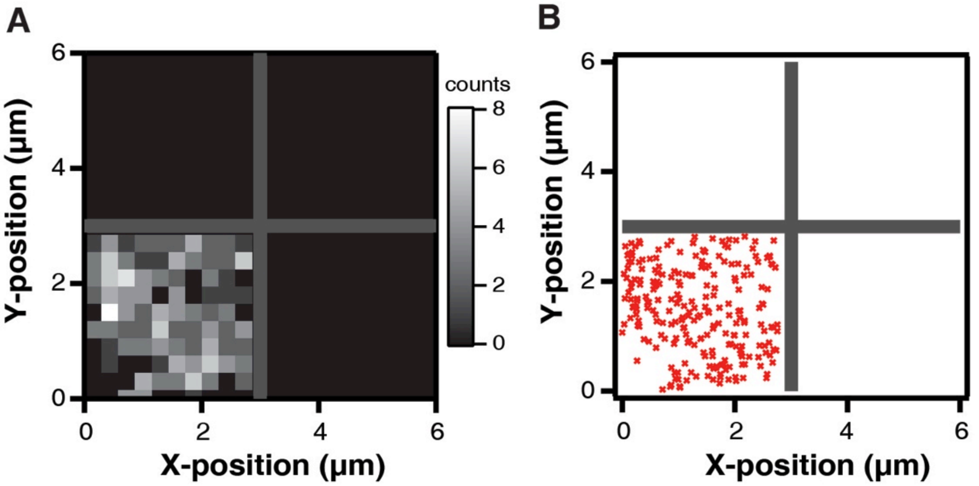

Fig. S4. SOScat-Atto647N diffuses uniformly within corrals.

(A) Greyscale density map showing how often a single SOScat-Atto647N visits a certain location in the bottom left corral; (B) In the corresponding localization map, each dot represents the location of SOScat-Atto647N identified by the tracking algorithm. The whole area shown contains 4 corrals, but only the bottom left corral has a SOScat-Atto647N molecule.

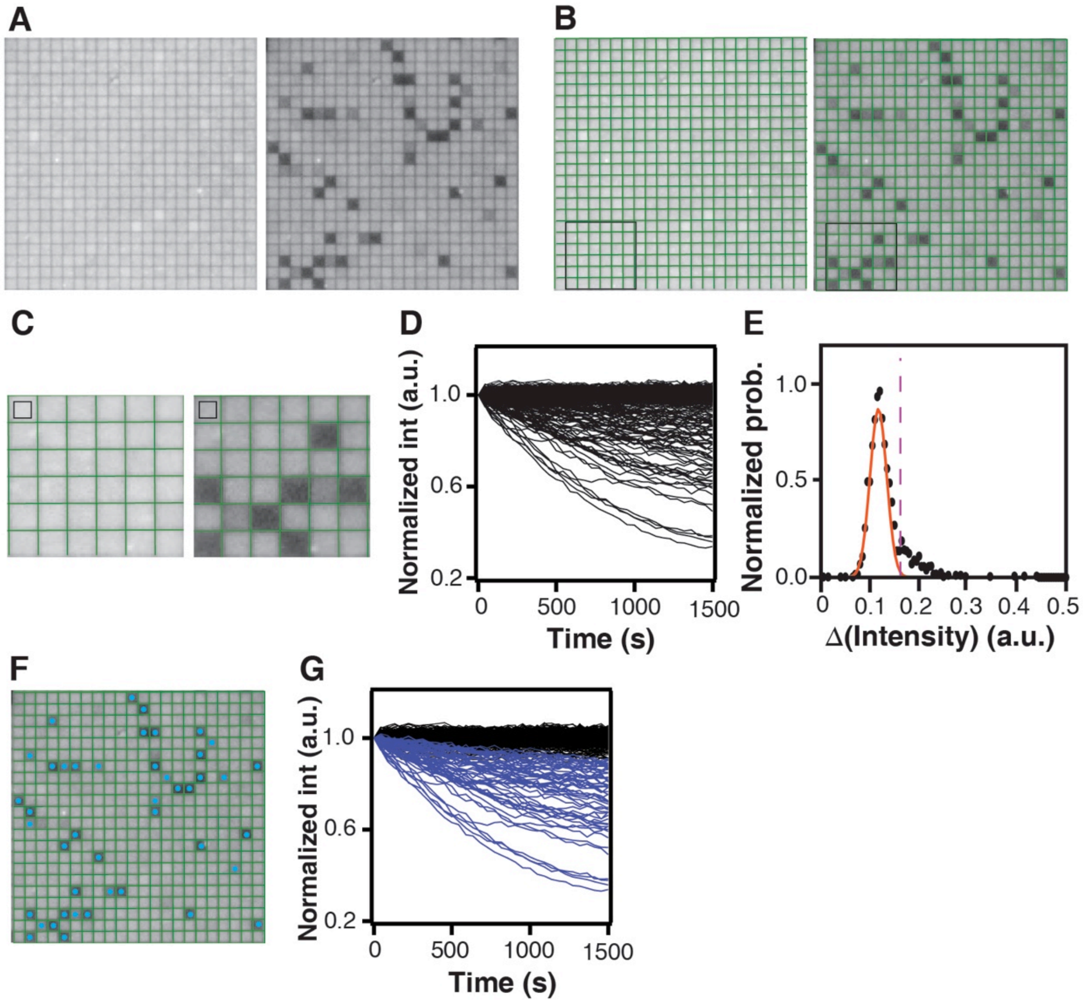

Fig. S5. Single molecule corral analysis.

(A) Flattened epifluorescence images of fluorescent nucleotide-loaded Ras in an array of 484 corrals before (left) and after (right) exchange reaction. (B) Using a custom algorithm in Matlab, the boundaries of corrals were defined and shown as green lines. (C) Zoomed-in images of (B). The black squares in the top-left corner of the images represent the region of interest when extracting fluorescence intensities from corrals. (D) Normalized and corrected intensity traces from individual corrals in the assay. (E) A distribution plot based on the intensity difference in each corral before and after the exchange reaction. The main peak corresponding to corrals without turnover (P2 population) was fitted to a Gaussian distribution (orange line). The threshold for selecting dark P1 corrals was set to allow less than 0.05% probability of overlap with the P2 population (vertical dotted line). (F) The automatic selection of dark P1 corrals (marked with light blue circles). (G) Corresponding kinetics traces belonging to either dark corrals (P1, blue) or corrals without SOS (P2, black). Corral size = 2x2 µm2.

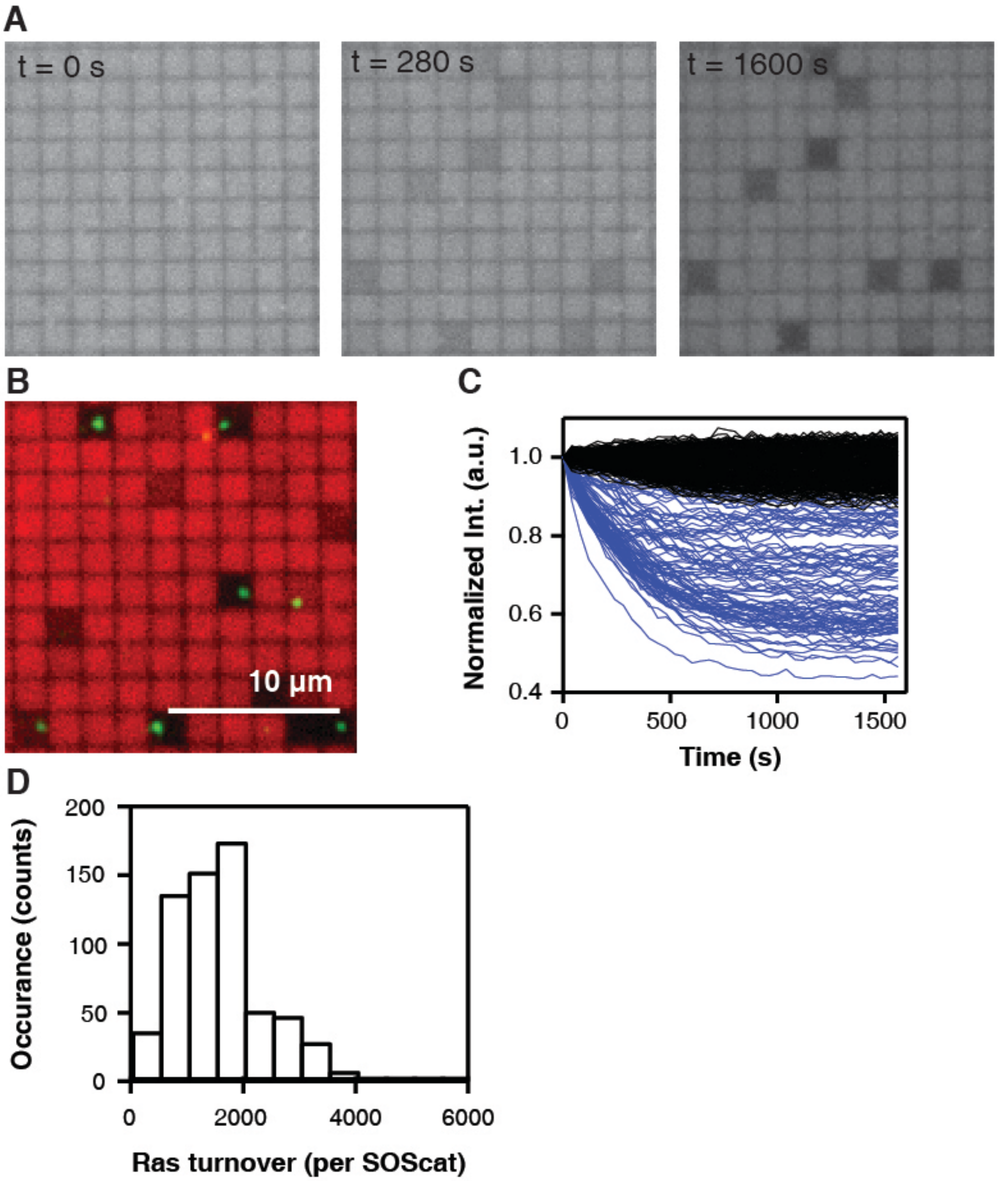

Fig. S6. Nucleotide exchange catalyzed by SOScat on double anchored Ras (Ras(C118S, 1-184)).

A Ras construct with two cysteines at 181 and 184 is functionalized onto the micro-patterned lipid bilayer. (A) Epifluorescence images of fluorescent nucleotide loaded Ras being catalyzed by SOScat at 3 different time points during the exchange reaction. (B) False color overlay of Ras (red) and labeled SOScat (SOScat-Atto647N; green) shows co-localization of dark corrals and a single SOScat. (C) Collection of kinetic traces from individual corrals with (blue traces) and without (black traces) enzymatic activity. (D) Histogram of total Ras-GTP-488 turnovers by individual SOS enzymes. Scale bars in (B) is 10µm.

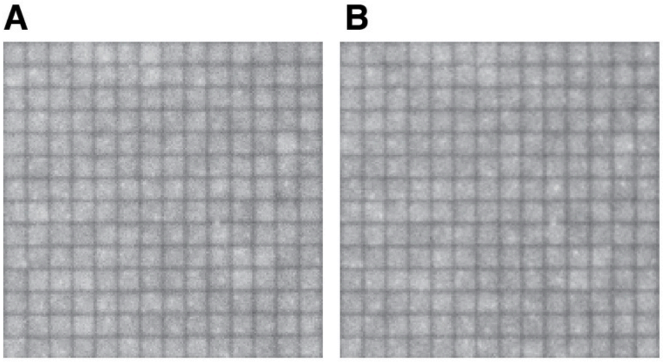

Fig. S7. SOScat(W729E) is non-processive.

Epifluorescence images of Ras nucleotide state (A) before and (B) 1000 s after SOScat(W729E) and non-fluorescent nucleotide was introduced into the corral assay. SOScat(W729E) was injected under identical conditions as SOScat but did not lead to the appearance of dark corrals, indicating that the mutant cannot mediate processive Ras turnover. Size of corral = 2x2 µm2.

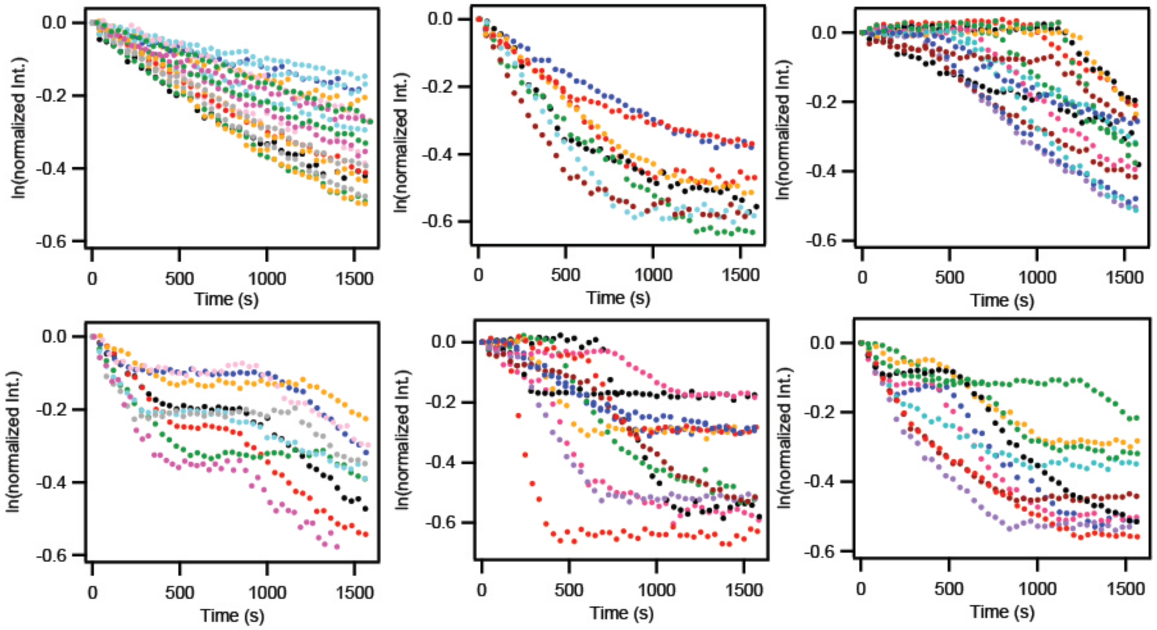

Fig. S8. Representative kinetic traces collected from individual corrals.

Total of 73 representative traces extracted from the single molecule assay are shown. All the trace is later analyzed by the change point algorithm as described in the materials and methods section.

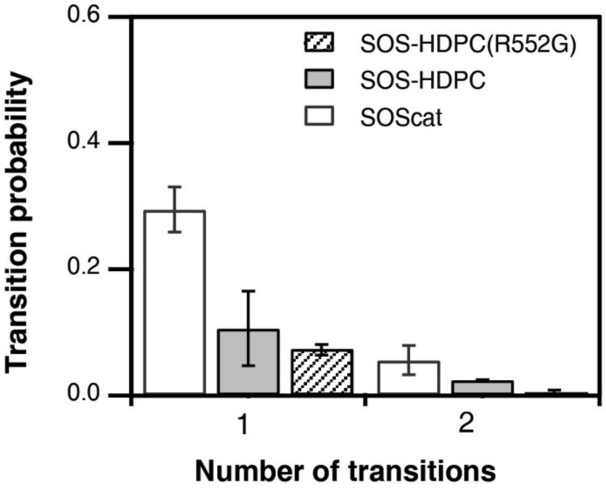

Fig. S9. N-terminal domains reduce the fluctuation frequency relative to SOScat.

State transition probabilities for SOScat (white block), SOS-HDPC (gray block) and SOS-HDPC(R552G) (patterned block), showing the likelihood of a given enzyme undergoing 1 or 2 state transitions during the experiment.

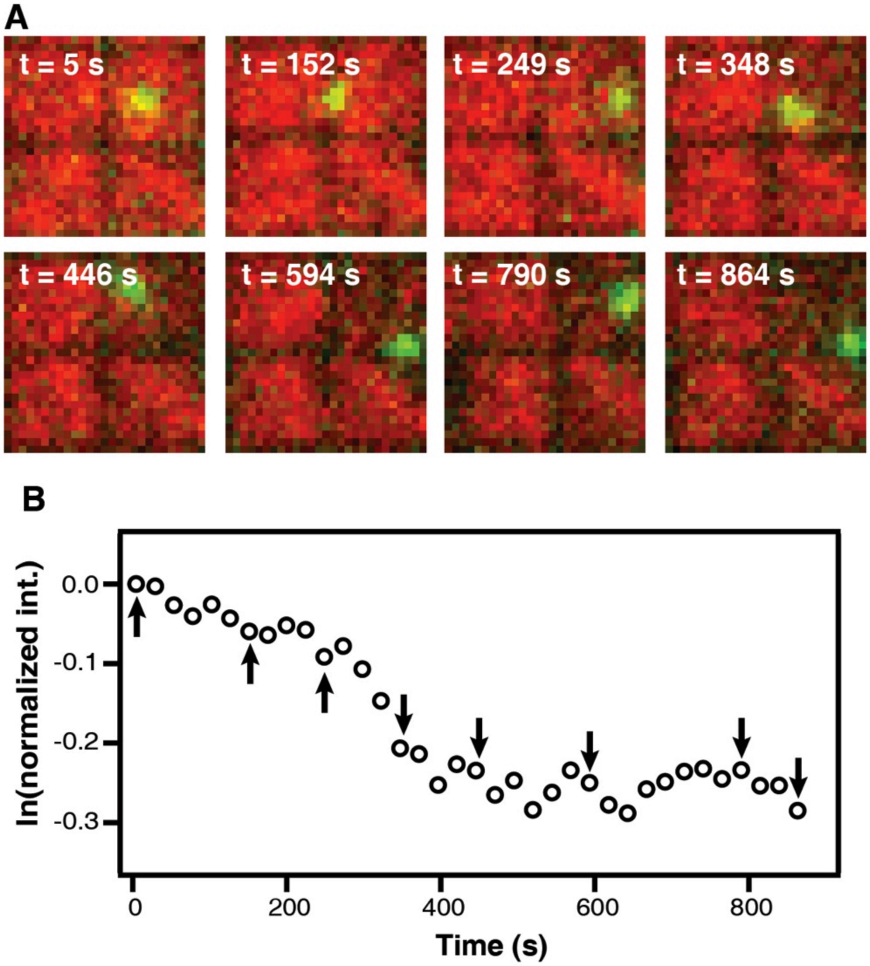

Fig. S10. Dynamic heterogeneity is not due to hindered SOScat diffusion.

(A) Simultaneous imaging of Ras turnover (red channel) and SOScat diffusion (green channel). Overlaid images show the decay of Ras fluorescence and the position of SOScat within the corral at various time points. SOScat was not immobile on the time-scale of catalytic rate switching. (B) The kinetic trace extracted from the corresponding corral (upper right) shows SOScat exhibited different catalytic rates during the course of the exchange reaction. Arrows indicate the corresponding time point shown in (A).

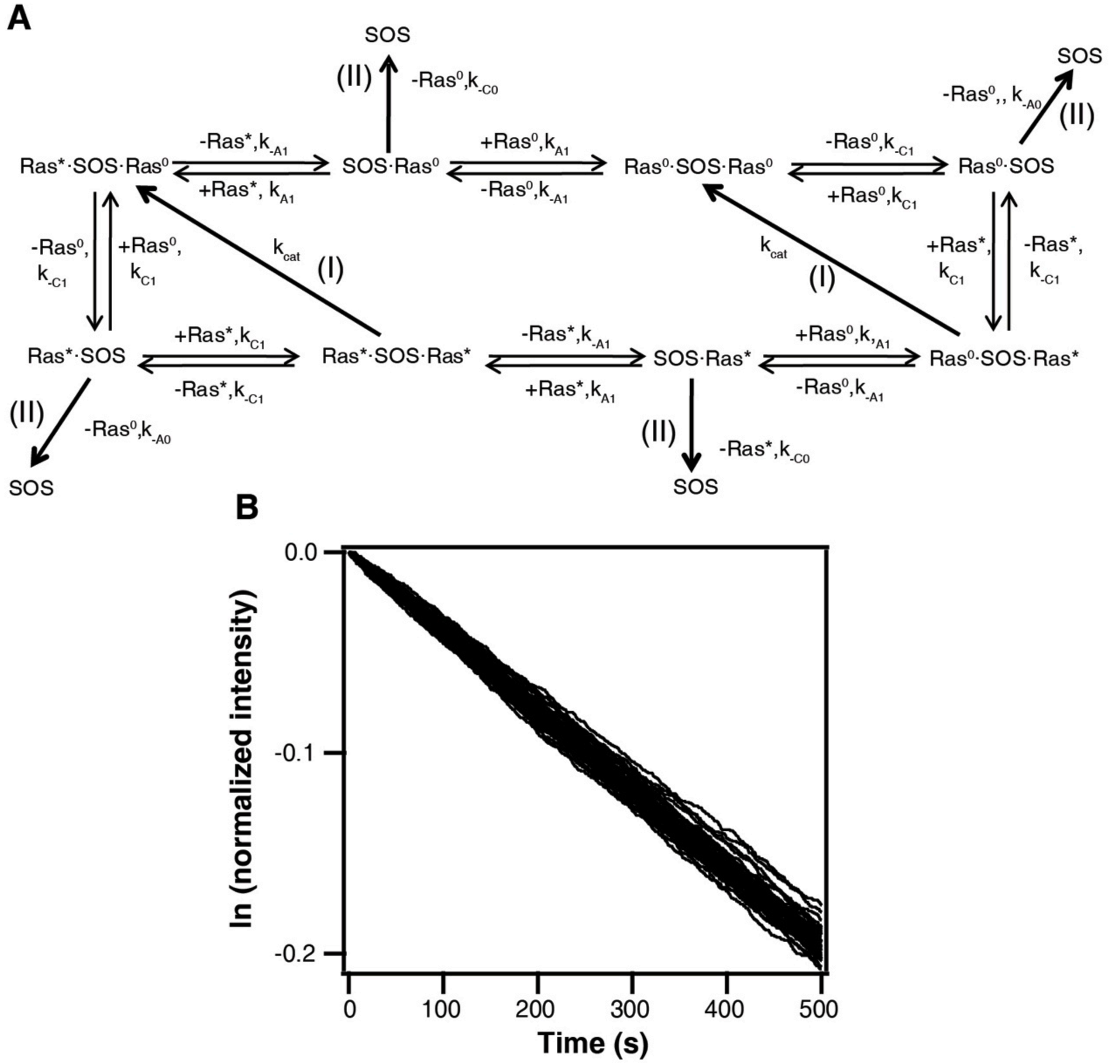
A
SOS
(II)
$-Ras^0,k_{-C0}$
SOS
$-Ras^0,, k_{-A0}$
(II)
$Ras^*\cdot SOS\cdot Ras^0$
$-Ras^*,k_{-A1}$
$+Ras^*, k_{A1}$
$SOS\cdot Ras^0$
$+Ras^0,k_{A1}$
$-Ras^0,k_{-A1}$
$Ras^0\cdot SOS\cdot Ras^0$
$-Ras^0,k_{-C1}$
$+Ras^0,k_{C1}$
$Ras^0\cdot SOS$
$-Ras^0, k_{-C1}$
$+Ras^0, k_{C1}$
k_{cat}
(I)
k_{cat}
(I)
$+Ras^*, k_{C1}$
$-Ras^*, k_{-C1}$
$Ras^*\cdot SOS$
$+Ras^*,k_{C1}$
$-Ras^*,k_{-C1}$
$Ras^*\cdot SOS\cdot Ras^*$
$-Ras^*,k_{-A1}$
$+Ras^*,k_{A1}$
$SOS\cdot Ras^*$
$+Ras^0,k,_{A1}$
$-Ras^0,k_{-A1}$
$Ras^0\cdot SOS\cdot Ras^*$
(II)
$-Ras^0,k_{-A0}$
SOS
(II)
$-Ras^*,k_{-C0}$
SOS
B
0.0
-0.1
-0.2
ln (normalized intensity)
0
100
200
300
400
500
Time (s)

Fig. S11. Stochastic variation in single-state SOS network.

(A) Reaction network for a single-state SOS molecule turning over Ras. Ras·SOS indicates Ras bound in the allosteric site, SOS·Ras indicates Ras bound in the catalytic site, and Ras·SOS·Ras indicates Ras in both allosteric and catalytic sites. Ras* represents a Ras loaded with fluorescent nucleotide whereas Ras0 is a Ras with non-fluorescent nucleotide. Channel (I) leads to a nucleotide exchange reaction and channel (II) describes the case where a SOS unbinds from the surface. (B) 50 representative kinetic traces obtained from stochastic simulation based on the reaction network in (A). Simulation condition: Time steps of 0.06 ms for 500 seconds. Ras density = 600 molecules/µm2.

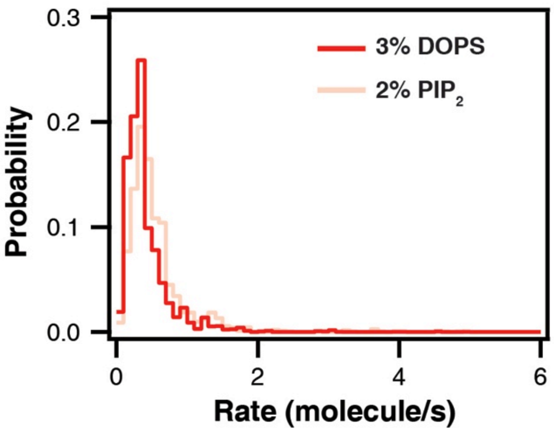

Fig. S12. PIP$_2$ does not activate the specific activity of SOS-HDPC.

Inclusion of 2% PIP$_2$ on the bilayer does not affect the observed rate of SOS-HDPC catalyzed Ras-GDP turnover (pink trace), in comparison to the 3% DOPS bilayer (red trace).

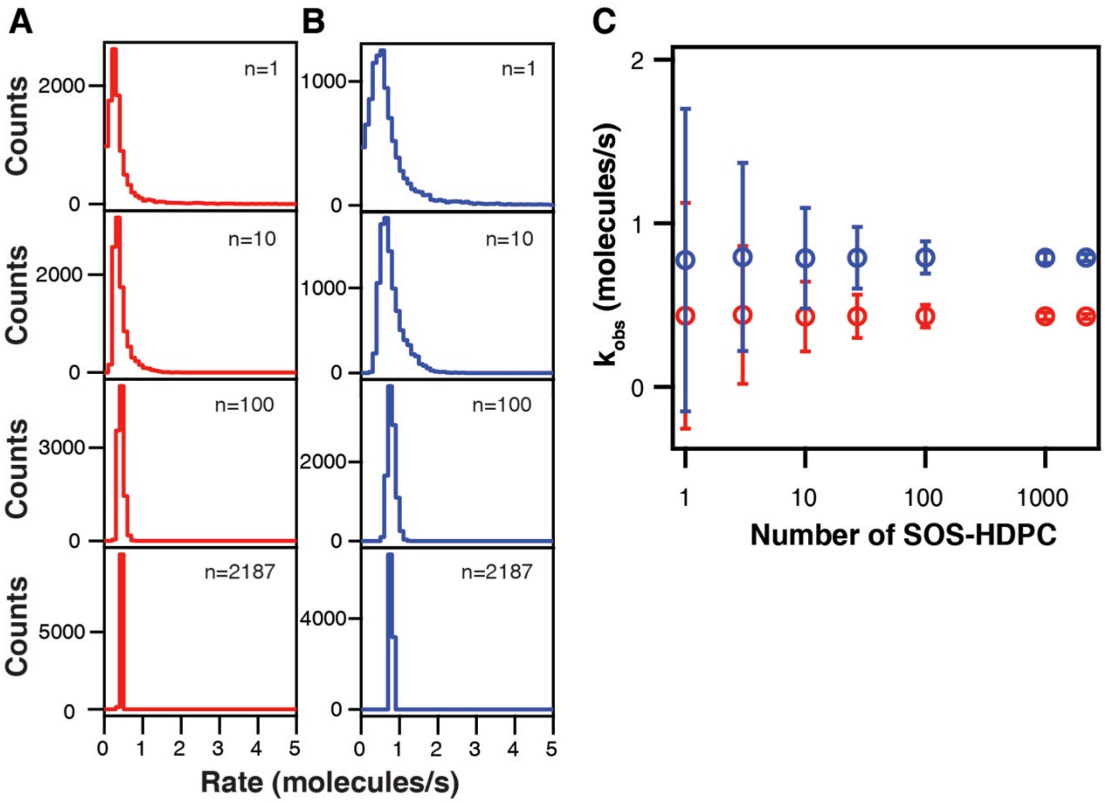

Fig. S13. SOS copy number and average catalytic rate.

(A) and (B) show distributions of average rate computed from Lorenzian fits to the experimental rate distributions. The average rate distributions are calculated for increasing sample sizes of SOS-HDPC with Ras-GDP (Red) or Ras-GTP (blue). (C) The mean rate constant kobs +/- the standard deviation from each average rate distribution is plotted for Ras-GDP (red) and Ras-GTP bound in SOS-HDPC.

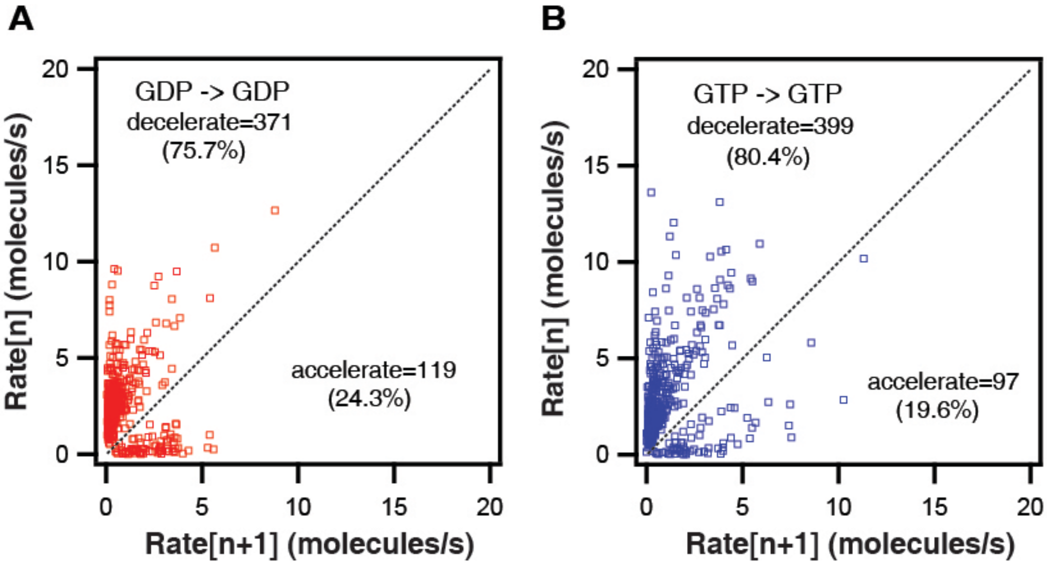

Fig. S14. Fluctuation path plots for SOScat.

For each state transition, the initial rate (n) is plotted against the subsequent state rate (n+1). Points above the diagonal correspond to rate decrease and vice versa. (A) Ras-GDP promotes SOScat fluctuations into lower activity states 76% of the time, primarily into a basal state with a rate close to 1 molecules/s-1. (B) Ras-GTP shows a similar pattern, albeit with a 4% shift toward fluctuations into lower activity states.

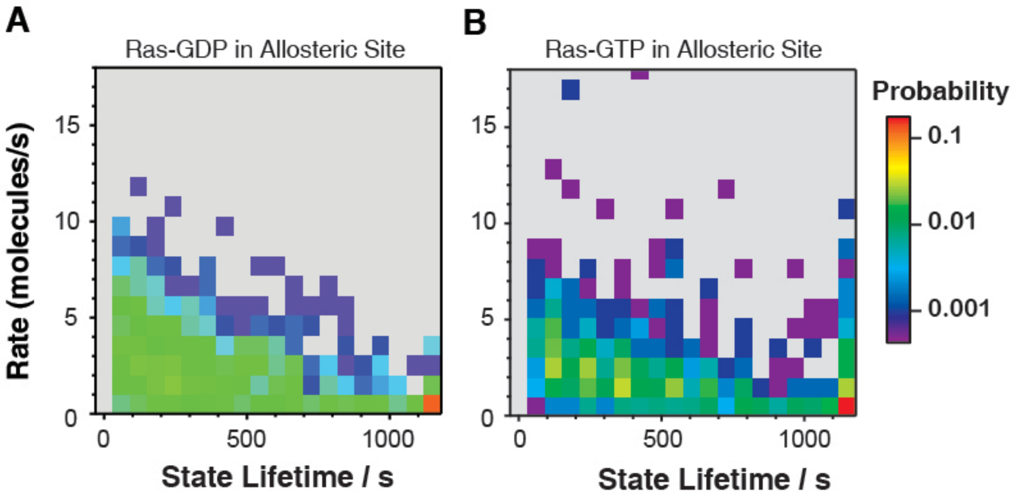

Fig. S15. Probability distribution maps of turnover rate and state lifetime observed in the single molecule assay.

Plots of turnover rates and state lifetime distribution from nucleotide exchange reactions catalyzed by SOScat when the allosteric site is bound with (A) Ras-GDP and (B) Ras-GDP, respectively.

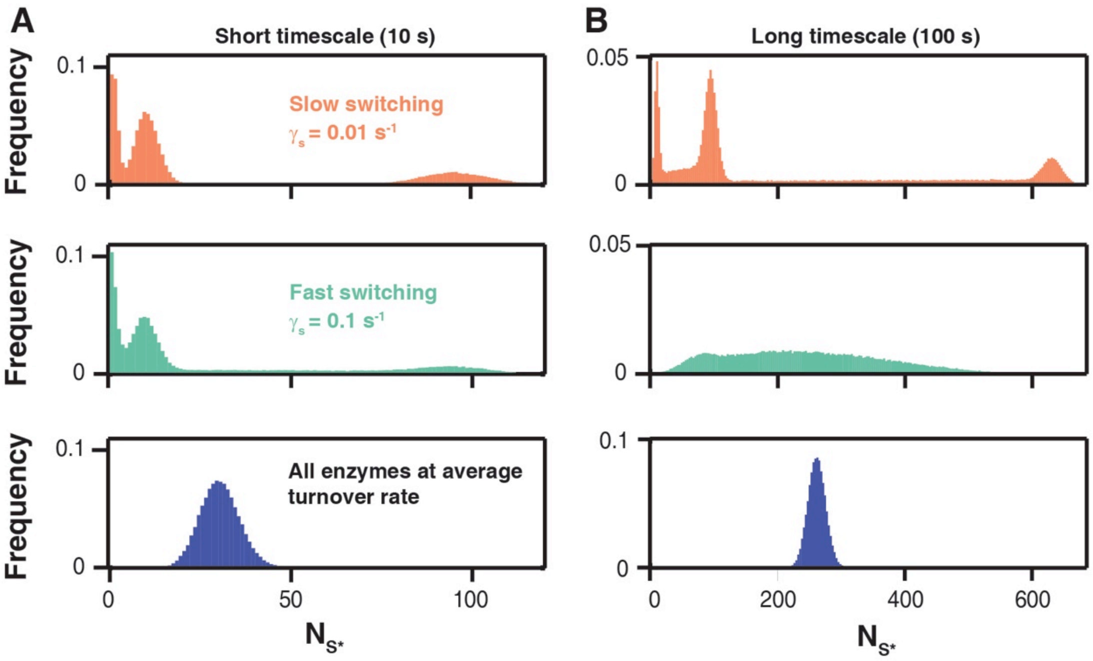

Fig. S16. Distribution of S^* as a function of switching rate and time.

Each row presents a different switching rate and each column presents a different time, with the first column (A) giving results at 10 s and the second column (B) giving results at 100 s. The first two rows use $p_1 = 0.25$, $p_2 = 0.5$, and $p_3 = 0.25$. The last row summarizes results for an enzyme the samples only the single, average rate of the first rows (0.003025 s-1). Each histogram summarizes the distribution of N_{s^*} from 105 independent trajectories. No deactivating enzymes are present.

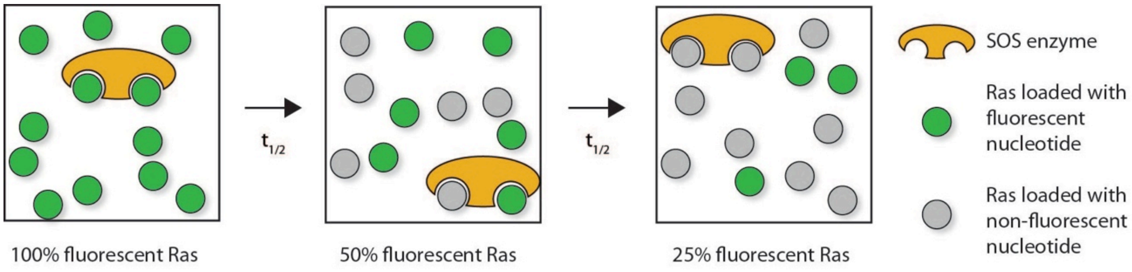
t1/2
t1/2
100% fluorescent Ras
50% fluorescent Ras
25% fluorescent Ras
SOS enzyme
Ras loaded with fluorescent nucleotide
Ras loaded with non-fluorescent nucleotide

Fig. S17. SOS activity and fluorescence decay in individual corrals.

During the enzymatic reaction, Ras and SOS surface concentrations remain constant within the corral. SOS activity exchanges fluorescent for non-fluorescent nucleotides in Ras, causing a decrease in fluorescence. Initially, when all Ras is fluorescent, the rate of Ras turnover and the rate of decrease of fluorescence are identical. As SOS begins spending more time turning over non-fluorescent Ras, the two rates diverge. Assuming that SOS does not distinguish between fluorescent and non-fluorescent Ras, the rate of turnover of total Ras will remain constant in a corral, while the rate of turnover of fluorescent Ras will decay exponentially.

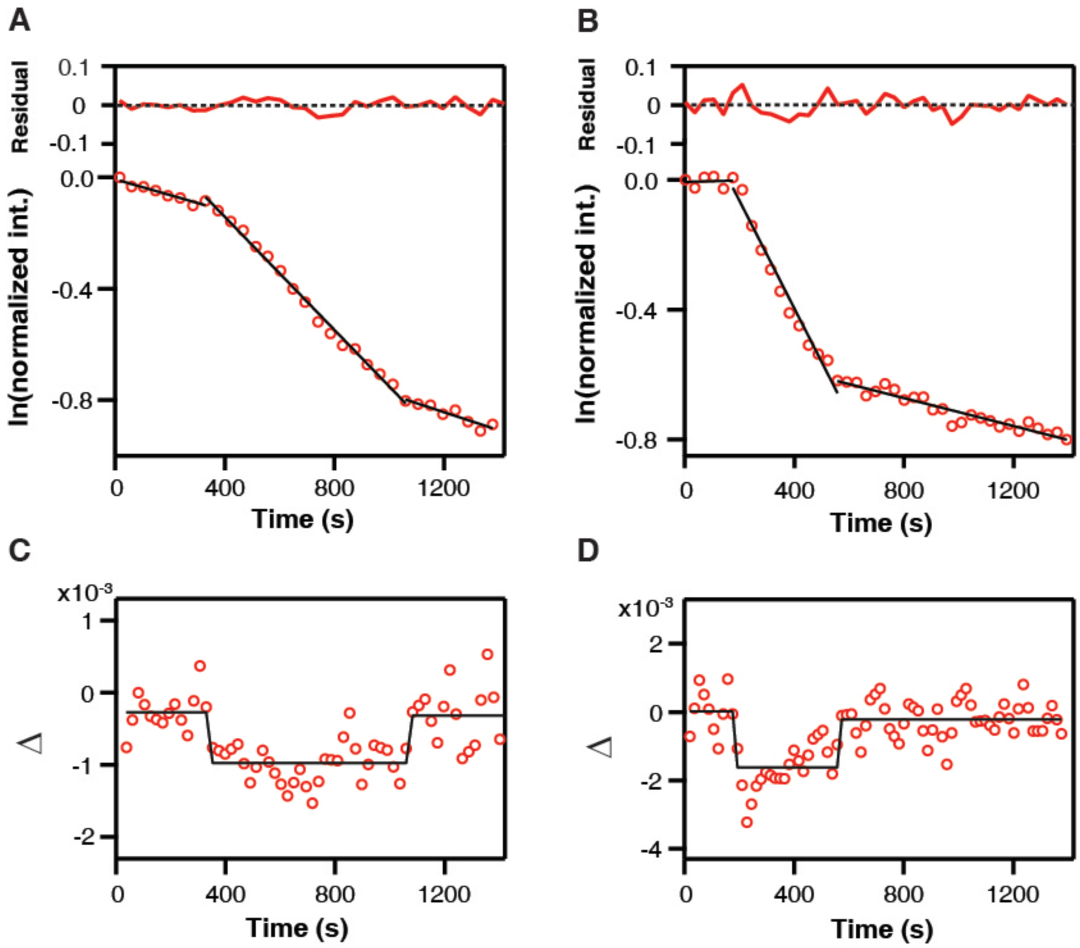

Fig. S18. Identification of individual functional states.

(A) and (B) Two representative kinetic traces and the identified kinetic states (black solid lines) are shown with fitting residuals plotted on top (red line). For the change point analysis, the traces were recast in the form of the local slope of the kinetic traces calculated as the difference between consecutive data points (Δ=(xi+1-xi)/(ti+1-ti), where i is a running variable looping through the trace and xi denotes the data point i in A and B). Such delta values were calculated for two neighboring points (i+1) but also for (i+2). (C) and (D) shows the traces corresponding to (A) and (B) recast in this way and the result of the change point identification (black solid lines).

Table S1: Reactions and rate constants used are adapted from (*8*)

Reaction	**k_{on} 1/(μM*s)**	**k_{off} (1/s)**	**k_{cat} (1/s)**
1. (allosteric binding) SOS(allo)+Ras-GDP↔SOS(allo)-Ras-GDP	.12	3.0	NA
2. (allosteric binding) SOS(allo)+Ras-GTP↔SOS(allo)-Ras-GTP	.11	.4	3.6
3. (deactivation by RasGAP) RasGAP+Ras-GTP↔RasGAP-Ras-GTP→RasGAP+Ras-GDP	1.74	.2	.1
4. (DAG binding of Rasgrp1) DAG+Rasgrp1↔DAG-Rasgrp1	5	5	1
5. (activation by Rasgrp1) DAG-Rasgrp1+Ras-GDP↔DAG-Rasgrp1-Ras-GDP→DAG-Rasgrp1 + Ras-GTP	.33	1.0	.01
6. (catalytic pocket reaction) SOS+Ras-GDP↔SOS-Ras-GDP	.27	4.0	.0005
7. (catalytic pocket binding when allosteric pocket is occupied by GDP) SOS(allo)-Ras-GDP + Ras-GDP ↔SOS(allo)-Ras-GDP-Ras-GDP	.07	1.0	(See Supplementary table S2a)
8. (catalytic pocket binding when allosteric pocket is occupied by GTP) SOS(allo)-Ras-GTP+Ras-GDP↔SOS(allo)-Ras-GTP-Ras-GDP	.05	.1	(See Supplementary table S2b)

Table S2a: Kcat distribution, SOS(allo)-Ras-GDP

	Kcat 1	**Kcat2**	**Kcat3**
Value (1/s)	.000545	.00545	
Probability	.5	.5	

Table S2b: Kcat distribution, SOS(allo)-Ras-GTP

	Kcat 1	**Kcat2**	**Kcat3**
Value (1/s)	.000545	.00545	.141
Probability	.25	.5	.25

Note: Kcat distributions are chosen such that the average Kcat value matches experimentally determined results previously used in the model (*8*).

Table S3: Rate switching reactions included.

In the table below, 'i' and 'j' will denote an arbitrary indexing over the various catalytic states of either SOS(allo)-Ras-GDP or SOS(allo)-Ras-GTP. Switching reactions are treated as first order reactions. A transition into state SOS(i) occurs with a rate K(switch)*P(i), where P(i) is the probability of SOS(i)'s catalytic rate. This is mathematically equivalent to each SOS enzyme switching its catalytic rate with rate K(switch) and then drawing a catalytic rate from the Kcat distribution listed above. K(on) and K(off) values referenced below are listed in Supplementary table 1 above. The value of K(switch) used has been varied between 1s^{-1} and .01 s^{-1}. In simulations for which the switching rate of SOS(allo)-Ras-GTP is slower than that of SOS(allo)-Ras-GDP, we have used a ten-fold difference in switch rates.

Reaction	**Rate**
SOS(i)(allo)-Ras-GDP→SOS(j)(allo)-Ras-GDP	K(switch)*P(j)
SOS(i)(allo)-Ras-GTP→SOS(j)(allo)-Ras-GTP	K(switch)*P(j)
SOS+Ras-GDP→SOS(i)(allo)-Ras-GDP	K(on)*P(i)
SOS+Ras-GTP→SOS(i)(allo)-Ras-GTP	K(on)*P(i)

Table S4: Concentrations used.

These concentrations have been shown to demonstrate bistability when Kcat fluctuation is not allowed (*8*).

Species	**Concentrations**
Ras	75 molecules/(μm)^2
SOS	Varied from 0 to 1900 molecules/(μm)^3
Rasgrp1	Varied from 0 to 1250 molecules/(μm)^3
DAG	12 molecules/(μm)^2
Ras-GAP	125 molecules/(μm)^3

Movie S1. Epifluorescence time lapse of SOScat-catalyzed nucleotide exchange reactions in the corral assay.

Immediately prior to capturing the movie, SOScat was injected as a pulse through the flow chamber. Flowing in non-fluorescent GTP then initiated the reaction, and the time-lapse imaging was started. Individual corrals are observed to gradually turn dark, as SOS within the corral exchanges fluorescent nucleotide with non-fluorescent nucleotide. The difference in fluorescence decay kinetics between corrals is visible by eye. The time interval per frame is 35 s (0.0286 Hz) and the total duration of the movie is 1365 s. The movie was recorded with 400 msec exposure time. Individual frames were aligned using the StackReg command of ImageJ.

Movie S2. TIRFM single molecule tracking of SOScat-Atto647N in corrals after the reaction.

False color overlay showing the epifluorescence emission from Ras-GTP-488 in red and the TIRFM emission from SOScat-Atto647N in green. A clear correspondence between dark corrals and SOScat enzymes is observed. The movie was recorded at ~5.5 Hz with 150 msec exposure time. The duration of movie is ~3.6 s (20 frames).

References and Notes

1. J. T. Groves, J. Kuriyan, Molecular mechanisms in signal transduction at the membrane. *Nat. Struct. Mol. Biol.* **17**, 659–665 (2010). Medline doi:10.1038/nsmb.1844

2. J. D. Scott, T. Pawson, Cell signaling in space and time: Where proteins come together and when they're apart. *Science* **326**, 1220–1224 (2009). Medline doi:10.1126/science.1175668

3. J. L. Bos, H. Rehmann, A. Wittinghofer, GEFs and GAPs: Critical elements in the control of small G proteins. *Cell* **129**, 865–877 (2007). Medline doi:10.1016/j.cell.2007.05.018

4. J. Cherfils, M. Zeghouf, Regulation of small GTPases by GEFs, GAPs, and GDIs. *Physiol. Rev.* **93**, 269–309 (2013). Medline doi:10.1152/physrev.00003.2012

5. A. Mor, M. R. Philips, Compartmentalized Ras/MAPK signaling. *Annu. Rev. Immunol.* **24**, 771–800 (2006). Medline doi:10.1146/annurev.immunol.24.021605.090723

6. S. M. Margarit, H. Sondermann, B. E. Hall, B. Nagar, A. Hoelz, M. Pirruccello, D. Bar-Sagi, J. Kuriyan, Structural evidence for feedback activation by Ras.GTP of the Ras-specific nucleotide exchange factor SOS. *Cell* **112**, 685–695 (2003). Medline doi:10.1016/S0092-8674(03)00149-1

7. S. Boykevisch, C. Zhao, H. Sondermann, P. Philippidou, S. Halegoua, J. Kuriyan, D. Bar-Sagi, Regulation of ras signaling dynamics by Sos-mediated positive feedback. *Curr. Biol.* **16**, 2173–2179 (2006). Medline doi:10.1016/j.cub.2006.09.033

8. J. Das, M. Ho, J. Zikherman, C. Govern, M. Yang, A. Weiss, A. K. Chakraborty, J. P. Roose, Digital signaling and hysteresis characterize ras activation in lymphoid cells. *Cell* **136**, 337–351 (2009). Medline doi:10.1016/j.cell.2008.11.051

9. J. E. Jun, I. Rubio, J. P. Roose, Regulation of Ras exchange factors and cellular localization of Ras activation by lipid messengers in T cells. *Front. Immunol.* **4**, 239 (2013). Medline doi:10.3389/fimmu.2013.00239

10. H. Sondermann, S. M. Soisson, S. Boykevisch, S. S. Yang, D. Bar-Sagi, J. Kuriyan, Structural analysis of autoinhibition in the Ras activator Son of sevenless. *Cell* **119**, 393–405 (2004). Medline doi:10.1016/j.cell.2004.10.005

11. K. K. Yadav, D. Bar-Sagi, Allosteric gating of Son of sevenless activity by the histone domain. *Proc. Natl. Acad. Sci. U.S.A.* **107**, 3436–3440 (2010). Medline doi:10.1073/pnas.0914315107

12. J. Gureasko, O. Kuchment, D. L. Makino, H. Sondermann, D. Bar-Sagi, J. Kuriyan, Role of the histone domain in the autoinhibition and activation of the Ras activator Son of Sevenless. *Proc. Natl. Acad. Sci. U.S.A.* **107**, 3430–3435 (2010). Medline doi:10.1073/pnas.0913915107

13. M. Tartaglia, L. A. Pennacchio, C. Zhao, K. K. Yadav, V. Fodale, A. Sarkozy, B. Pandit, K. Oishi, S. Martinelli, W. Schackwitz, A. Ustaszewska, J. Martin, J. Bristow, C. Carta, F. Lepri, C. Neri, I. Vasta, K. Gibson, C. J. Curry, J. P. Siguero, M. C. Digilio, G. Zampino, B. Dallapiccola, D. Bar-Sagi, B. D. Gelb, Gain-of-function SOS1 mutations cause a

distinctive form of Noonan syndrome. *Nat. Genet.* **39**, 75–79 (2007). Medline doi:10.1038/ng1939

14. E. Korobkova, T. Emonet, J. M. Vilar, T. S. Shimizu, P. Cluzel, From molecular noise to behavioural variability in a single bacterium. *Nature* **428**, 574–578 (2004). Medline doi:10.1038/nature02404

15. D. J. Irvine, M. A. Purbhoo, M. Krogsgaard, M. M. Davis, Direct observation of ligand recognition by T cells. *Nature* **419**, 845–849 (2002). Medline doi:10.1038/nature01076

16. B. N. Manz, B. L. Jackson, R. S. Petit, M. L. Dustin, J. Groves, T-cell triggering thresholds are modulated by the number of antigen within individual T-cell receptor clusters. *Proc. Natl. Acad. Sci. U.S.A.* **108**, 9089–9094 (2011). Medline doi:10.1073/pnas.1018771108

17. G. P. O'Donoghue, R. M. Pielak, A. A. Smoligovets, J. J. Lin, J. T. Groves, Direct single molecule measurement of TCR triggering by agonist pMHC in living primary T cells. *eLife* **2**, e00778 (2013). Medline doi:10.7554/eLife.00778

18. P. J. Choi, L. Cai, K. Frieda, X. S. Xie, A stochastic single-molecule event triggers phenotype switching of a bacterial cell. *Science* **322**, 442–446 (2008). Medline doi:10.1126/science.1161427

19. J. Gureasko, W. J. Galush, S. Boykevisch, H. Sondermann, D. Bar-Sagi, J. T. Groves, J. Kuriyan, Membrane-dependent signal integration by the Ras activator Son of sevenless. *Nat. Struct. Mol. Biol.* **15**, 452–461 (2008). Medline doi:10.1038/nsmb.1418

20. Materials and methods are available as supplementary materials on *Science* Online.

21. J. T. Groves, N. Ulman, S. G. Boxer, Micropatterning fluid lipid bilayers on solid supports. *Science* **275**, 651–653 (1997). Medline doi:10.1126/science.275.5300.651

22. J. T. Groves, R. Parthasarathy, M. B. Forstner, Fluorescence imaging of membrane dynamics. *Annu. Rev. Biomed. Eng.* **10**, 311–338 (2008). Medline doi:10.1146/annurev.bioeng.10.061807.160431

23. D. L. Ensign, V. S. Pande, Bayesian detection of intensity changes in single molecule and molecular dynamics trajectories. *J. Phys. Chem. B* **114**, 280–292 (2010). Medline doi:10.1021/jp906786b

24. D. D. Boehr, R. Nussinov, P. E. Wright, The role of dynamic conformational ensembles in biomolecular recognition. *Nat. Chem. Biol.* **5**, 789–796 (2009). Medline doi:10.1038/nchembio.232

25. K. Henzler-Wildman, D. Kern, Dynamic personalities of proteins. *Nature* **450**, 964–972 (2007). Medline doi:10.1038/nature06522

26. K. A. Henzler-Wildman, M. Lei, V. Thai, S. J. Kerns, M. Karplus, D. Kern, A hierarchy of timescales in protein dynamics is linked to enzyme catalysis. *Nature* **450**, 913–916 (2007). Medline doi:10.1038/nature06407

27. W. Min, G. Luo, B. J. Cherayil, S. C. Kou, X. S. Xie, Observation of a power-law memory kernel for fluctuations within a single protein molecule. *Phys. Rev. Lett.* **94**, 198302 (2005). Medline doi:10.1103/PhysRevLett.94.198302

28. C. Zhao, G. Du, K. Skowronek, M. A. Frohman, D. Bar-Sagi, Phospholipase D2-generated phosphatidic acid couples EGFR stimulation to Ras activation by Sos. *Nat. Cell Biol.* **9**, 706–712 (2007). Medline doi:10.1038/ncb1594

29. A. del Sol, C. J. Tsai, B. Ma, R. Nussinov, The origin of allosteric functional modulation: Multiple pre-existing pathways. *Structure* **17**, 1042–1050 (2009). Medline doi:10.1016/j.str.2009.06.008

30. J. P. Changeux, Allostery and the Monod-Wyman-Changeux model after 50 years. *Annu. Rev. Biophys.* **41**, 103–133 (2012). Medline doi:10.1146/annurev-biophys-050511-102222

31. P. Csermely, R. Palotai, R. Nussinov, Induced fit, conformational selection and independent dynamic segments: An extended view of binding events. *Trends Biochem. Sci.* **35**, 539–546 (2010). Medline doi:10.1016/j.tibs.2010.04.009

32. J. Güldenhaupt, T. Rudack, P. Bachler, D. Mann, G. Triola, H. Waldmann, C. Kötting, K. Gerwert, N-Ras forms dimers at POPC membranes. *Biophys. J.* **103**, 1585–1593 (2012). Medline doi:10.1016/j.bpj.2012.08.043

33. D. T. Gillespie, A general method for numerically simulating the stochastic time evolution of coupled chemical reactions. *J. Comput. Phys.* **22**, 403–434 (1976). doi:10.1016/0021-9991(76)90041-3

34. N. C. Hartman, J. T. Groves, Signaling clusters in the cell membrane. *Curr. Opin. Cell Biol.* **23**, 370–376 (2011). Medline doi:10.1016/j.ceb.2011.05.003

35. A. S. Harding, J. F. Hancock, Using plasma membrane nanoclusters to build better signaling circuits. *Trends Cell Biol.* **18**, 364–371 (2008). Medline doi:10.1016/j.tcb.2008.05.006

36. B. N. Kholodenko, J. F. Hancock, W. Kolch, Signalling ballet in space and time. *Nat. Rev. Mol. Cell Biol.* **11**, 414–426 (2010). Medline doi:10.1038/nrm2901

37. H. Wu, Higher-order assemblies in a new paradigm of signal transduction. *Cell* **153**, 287–292 (2013). Medline doi:10.1016/j.cell.2013.03.013

38. H. E. Grecco, M. Schmick, P. I. Bastiaens, Signaling from the living plasma membrane. *Cell* **144**, 897–909 (2011). Medline doi:10.1016/j.cell.2011.01.029

39. J. E. Purvis, G. Lahav, Encoding and decoding cellular information through signaling dynamics. *Cell* **152**, 945–956 (2013). Medline doi:10.1016/j.cell.2013.02.005

40. H. P. Lu, L. Xun, X. S. Xie, Single-molecule enzymatic dynamics. *Science* **282**, 1877–1882 (1998). Medline doi:10.1126/science.282.5395.1877

41. B. P. English, W. Min, A. M. van Oijen, K. T. Lee, G. Luo, H. Sun, B. J. Cherayil, S. C. Kou, X. S. Xie, Ever-fluctuating single enzyme molecules: Michaelis-Menten equation revisited. *Nat. Chem. Biol.* **2**, 87–94 (2006). Medline doi:10.1038/nchembio759

42. M. K. Prakash, R. A. Marcus, An interpretation of fluctuations in enzyme catalysis rate, spectral diffusion, and radiative component of lifetimes in terms of electric field fluctuations. *Proc. Natl. Acad. Sci. U.S.A.* **104**, 15982–15987 (2007). Medline doi:10.1073/pnas.0707859104

43. W. J. Albery, J. R. Knowles, Evolution of enzyme function and the development of catalytic efficiency. *Biochemistry* **15**, 5631–5640 (1976). Medline doi:10.1021/bi00670a032

44. J. P. Roose, M. Mollenauer, M. Ho, T. Kurosaki, A. Weiss, Unusual interplay of two types of Ras activators, RasGRP and SOS, establishes sensitive and robust Ras activation in lymphocytes. *Mol. Cell. Biol.* **27**, 2732–2745 (2007). Medline doi:10.1128/MCB.01882-06

45. P. M. Nair, K. Salaita, R. S. Petit, J. T. Groves, Using patterned supported lipid membranes to investigate the role of receptor organization in intercellular signaling. *Nat. Protoc.* **6**, 523–539 (2011). Medline doi:10.1038/nprot.2011.302

46. H. Sondermann, B. Nagar, D. Bar-Sagi, J. Kuriyan, Computational docking and solution x-ray scattering predict a membrane-interacting role for the histone domain of the Ras activator son of sevenless. *Proc. Natl. Acad. Sci. U.S.A.* **102**, 16632–16637 (2005). Medline doi:10.1073/pnas.0508315102

47. A. Fischer, M. Hekman, J. Kuhlmann, I. Rubio, S. Wiese, U. R. Rapp, B- and C-RAF display essential differences in their binding to Ras: The isotype-specific N terminus of B-RAF facilitates Ras binding. *J. Biol. Chem.* **282**, 26503–26516 (2007). Medline doi:10.1074/jbc.M607458200

48. K. Kuhn, D. J. Owen, B. Bader, A. Wittinghofer, J. Kuhlmann, H. Waldmann, Synthesis of functional Ras lipoproteins and fluorescent derivatives. *J. Am. Chem. Soc.* **123**, 1023–1035 (2001). Medline doi:10.1021/ja002723o

49. L. Brunsveld, J. Kuhlmann, H. Waldmann, Synthesis of palmitoylated Ras-peptides and -proteins. *Methods* **40**, 151–165 (2006). Medline doi:10.1016/j.ymeth.2006.04.014

50. S. B. Triffo, H. H. Huang, A. W. Smith, E. T. Chou, J. T. Groves, Monitoring lipid anchor organization in cell membranes by PIE-FCCS. *J. Am. Chem. Soc.* **134**, 10833–10842 (2012). Medline doi:10.1021/ja300374c

51. J. D. Müller, Y. Chen, E. Gratton, Resolving heterogeneity on the single molecular level with the photon-counting histogram. *Biophys. J.* **78**, 474–486 (2000). Medline doi:10.1016/S0006-3495(00)76610-0

52. S. C. Kou, B. J. Cherayil, W. Min, B. P. English, X. S. Xie, Single-molecule Michaelis-Menten equations. *J. Phys. Chem. B* **109**, 19068–19081 (2005). Medline doi:10.1021/jp051490q

53. A. A. Gorfe, M. Hanzal-Bayer, D. Abankwa, J. F. Hancock, J. A. McCammon, Structure and dynamics of the full-length lipid-modified H-Ras protein in a 1,2-dimyristoylglycero-3-phosphocholine bilayer. *J. Med. Chem.* **50**, 674–684 (2007). Medline doi:10.1021/jm061053f

54. H. Heller, M. Schaefer, K. Schulten, Molecular dynamics simulation of a bilayer of 200 lipids in the gel and in the liquid crystal phase. *J. Phys. Chem.* **97**, 8343–8360 (1993). doi:10.1021/j100133a034

55. T. S. Freedman, H. Sondermann, G. D. Friedland, T. Kortemme, D. Bar-Sagi, S. Marqusee, J. Kuriyan, A Ras-induced conformational switch in the Ras activator Son of sevenless.

Proc. Natl. Acad. Sci. U.S.A. **103**, 16692–16697 (2006). Medline doi:10.1073/pnas.0608127103

56. R. G. Smock, L. M. Gierasch, Sending signals dynamically. *Science* **324**, 198–203 (2009). Medline doi:10.1126/science.1169377
57. S. R. Tzeng, C. G. Kalodimos, Dynamic activation of an allosteric regulatory protein. *Nature* **462**, 368–372 (2009). Medline doi:10.1038/nature08560
58. S. R. Tzeng, C. G. Kalodimos, Protein activity regulation by conformational entropy. *Nature* **488**, 236–240 (2012). Medline doi:10.1038/nature11271
59. P. Li, I. R. Martins, G. K. Amarasinghe, M. K. Rosen, Internal dynamics control activation and activity of the autoinhibited Vav DH domain. *Nat. Struct. Mol. Biol.* **15**, 613–618 (2008). Medline doi:10.1038/nsmb.1428
60. T. S. Freedman, H. Sondermann, O. Kuchment, G. D. Friedland, T. Kortemme, J. Kuriyan, Differences in flexibility underlie functional differences in the Ras activators son of sevenless and Ras guanine nucleotide releasing factor 1. *Structure* **17**, 41–53 (2009). Medline doi:10.1016/j.str.2008.11.004
61. C. Frieden, Slow transitions and hysteretic behavior in enzymes. *Annu. Rev. Biochem.* **48**, 471–489 (1979). Medline doi:10.1146/annurev.bi.48.070179.002351
62. E. Leikina, C. Ramos, I. Markovic, J. Zimmerberg, L. V. Chernomordik, Reversible stages of the low-pH-triggered conformational change in influenza virus hemagglutinin. *EMBO J.* **21**, 5701–5710 (2002). Medline doi:10.1093/emboj/cdf559
63. A. Behzadi, R. Hatleskog, P. Ruoff, Hysteretic enzyme adaptation to environmental pH: Change in storage pH of alkaline phosphatase leads to a pH-optimum in the opposite direction to the applied change. *Biophys. Chem.* **77**, 99–109 (1999). Medline doi:10.1016/S0301-4622(99)00013-7
64. O. Rocks, A. Peyker, P. I. Bastiaens, Spatio-temporal segregation of Ras signals: One ship, three anchors, many harbors. *Curr. Opin. Cell Biol.* **18**, 351–357 (2006). Medline doi:10.1016/j.ceb.2006.06.007
65. A. Kusumi, C. Nakada, K. Ritchie, K. Murase, K. Suzuki, H. Murakoshi, R. S. Kasai, J. Kondo, T. Fujiwara, Paradigm shift of the plasma membrane concept from the two-dimensional continuum fluid to the partitioned fluid: High-speed single-molecule tracking of membrane molecules. *Annu. Rev. Biophys. Biomol. Struct.* **34**, 351–378 (2005). Medline doi:10.1146/annurev.biophys.34.040204.144637
66. H. Murakoshi, R. Iino, T. Kobayashi, T. Fujiwara, C. Ohshima, A. Yoshimura, A. Kusumi, Single-molecule imaging analysis of Ras activation in living cells. *Proc. Natl. Acad. Sci. U.S.A.* **101**, 7317–7322 (2004). Medline doi:10.1073/pnas.0401354101
67. J. F. Hancock, R. G. Parton, Ras plasma membrane signalling platforms. *Biochem. J.* **389**, 1–11 (2005). Medline doi:10.1042/BJ20050231
68. D. Abankwa, A. A. Gorfe, J. F. Hancock, Ras nanoclusters: Molecular structure and assembly. *Semin. Cell Dev. Biol.* **18**, 599–607 (2007). Medline doi:10.1016/j.semcdb.2007.08.003

69. M. Kofer-Geles, I. Gottfried, R. Haklai, G. Elad-Zefadia, Y. Kloog, U. Ashery, Rasosomes spread Ras signals from plasma membrane 'hotspots'. *Biochim. Biophys. Acta* **1793**, 1691–1702 (2009). Medline doi:10.1016/j.bbamcr.2009.08.004